

Electronic Supplementary Information for:

**Enhancing Catalytic Alkane Hydroxylation by Tuning the
Outer Coordination Sphere in a Heme-Containing Metal–
Organic Framework**

David Z. Zee¹ and T. David Harris*^{1,2}

*¹Department of Chemistry, Northwestern University, 2145 Sheridan Road,
Evanston IL 60208, United States*

*²Department of Chemistry, University of California, Berkeley,
Berkeley, California 94720, United States*

Email: dharris@berkeley.edu

Chem. Sci.

Table of Contents

Experimental Section	S3
Figure S1. ^1H NMR spectra of acid-digested as-synthesized PCN-224, 1 , and 2	S9
Table S1. Quantification of $[\text{TCCP}]^{4-}$ to acetate, formate, and benzoate in MOFs	S10
Figure S2. Methyl acetate formation from methanol and 1	S11
Figure S3. PXRD patterns of as-synthesized PCN-224, 1 , 2 , 1FeCl , and 2FeCl	S12
Figure S4. Diffuse reflectance UV-vis spectra of 1 , 2 , and tetraphenylporphyrin	S13
Figure S5. Diffuse reflectance UV-vis spectra of 1FeCl , 2FeCl , and (TPP)FeCl	S14
Figure S6. Zero-field ^{57}Fe Mössbauer spectra of (TPP)FeCl, 1FeCl , and 2FeCl	S15
Table S2. Fit parameters for the zero-field ^{57}Fe Mössbauer spectra of (TPP)FeCl, 1FeCl , and 2FeCl	S16
Table S3. Crystallographic details for frameworks 1 , 1FeCl , and 2	S17
Figure S7–9. Thermal ellipsoid plots of 1 , 1FeCl , and 2	S18–20
Figure S10. Disorder of the bridging oxygen atoms in the Zr_6 cluster in 1	S21
Figure S11. Single-crystal X-ray structure of the $[\text{Zr}_6\text{O}_4(\text{OH})_4(\text{CH}_3\text{CO}_2)_6]^{6+}$ cluster in 1 , depicting the μ -acetate and κ^2 -acetate binding modes	S22
Table S4. Terminal $\text{Zr}-\text{OH}$ and $\text{Zr}-\text{OH}_2$ bond distances in crystallographically characterized 7-coordinate Zr^{4+} ions	S23
Figure S12. Full DRIFTS spectra of frameworks 1 , 2 , 1FeCl and 2FeCl	S24
Figure S13. Nitrogen isotherms for frameworks 1 , 2 , 1FeCl , and 2FeCl at 77 K	S25
Figure S14–17. Determination of the BET surface areas for 1 , 2 , 1FeCl , and 2FeCl	S26–29
Table S5. Parameters and consistency criteria checks for BET surface areas	S30
Table S6. Calculated N_2 -accessible surface areas of frameworks 1 , 2 , and 1FeCl	S30
Table S7. Yields of cyclohexanol, cyclohexanone, and chlorocyclohexane in catalytic cyclohexane oxidation with iodosylbenzene	S31
Table S8. Comparative activities of Fe and Mn porphyrin framework-based catalysts for cyclohexane oxidation	S32
Table S9. Yields of cyclohexanol, cyclohexanone, and chlorocyclohexane in catalytic cyclohexane oxidation with 2- <i>tert</i> -butylsulfonyliodosylbenzene	S33
References	S34

Experimental Section

Materials and Methods. Unless otherwise stated, all manipulations were performed under a dinitrogen atmosphere using either a Vacuum Atmospheres Nexus II glovebox (<1 ppm O₂, <0.5 ppm H₂O) or a dual-manifold high-vacuum (10⁻⁵–10⁻⁶ Torr) line. The solvents *N,N*-dimethylformamide (DMF), dichloromethane, and diethyl ether (Et₂O) were deoxygenated by purging with argon for 45 mins, dried using a commercial solvent purification system from Pure Process Technology, and stored under a dinitrogen atmosphere over activated 3 Å molecular sieves. All other solvents were purchased from Fisher Chemical and used as received.

Zirconium tetrachloride (Alfa Aesar, >99.5% metals basis), iron(III) chloride (Strem, anhydrous, 98%), and tetrabutylammonium acetate (MilliporeSigma, 97%) were stored in a glovebox and used without further purification. Benzoic acid (Alfa Aesar, 99%), *N,O*-bis(trimethylsilyl)acetamide (Oakwood Chemicals, 95%) were used as received. Acetic anhydride (Ac₂O, Alfa Aesar, >99%) and acetic acid (Fisher Chemical, Certified ACS) were used as received or degassed by three freeze-pump-thaw cycles before using in a glovebox. The compound 2,6-lutidine (Alfa Aesar, 98+%) was stirred over aluminum trichloride (~0.7 g per 5 mL of lutidine) under N₂ for 2 h at ambient temperature,¹ then distilled under N₂, and stored over activated 3 Å molecular sieves before use. Cyclohexane (MilliporeSigma, 99%) was washed with concentrated H₂SO₄ to remove trace cyclohexene,¹ separated, distilled under N₂, and stored over activated 3 Å molecular sieves before use.

Literature Compounds. The compounds tetrakis(4-carboxyphenyl)porphyrin (H₆TCPP),² tetraphenylporphyrin (H₂TPP),³ and tetraphenylporphyrin iron(III) chloride (TPPFeCl)² were synthesized according to literature procedures. The compound iodosylbenzene was prepared by oxidation of iodobenzene with sodium perborate tetrahydrate,⁴ followed by alkaline hydrolysis of (diacetoxyiodo)benzene.⁵ The compound 2-*tert*-butylsulfonyliodosylbenzene was prepared by biphasic chlorination of 2-*tert*-butylsulfonyliodobenzene with KClO₃ and alkaline hydrolysis of the iodobenzene dichloride.⁶

(H₂TCPP)₃{Zr₆O₄(OH)₄(CH₃CO₂)₆}₂, PCN-224' (1). This preparation was performed under air. A 1-L cylindrical glass bottle was charged with *ca.* 3 mL of *N,O*-bis(trimethylsilyl)acetamide, sealed with a Teflon-lined, GL 45 thread screw cap, and heated to 130 °C in an oven for 1 h. The bottle was then allowed to cool to room temperature, rinsed with acetone, and dried. Zirconium tetrachloride (4.94 g, 21.2 mmol) and DMF (350 mL) were added to the glass bottle, and the mixture was sonicated for 1 h to yield a clear solution. Benzoic acid (77.7 g, 636 mmol) was added, and the mixture was sonicated for 1 h to give a clear solution. The ligand H₆TCPP (1.68 g, 2.12 mmol) and deionized water (1.15 g, 63.6 mmol) were added, and the mixture was sonicated for 1 h to give a green suspension with a total volume of *ca.* 450 mL. The mixture was then heated to 130 °C in an oven for 72 h to give a purple crystalline solid in a dark red-brown solution. The solution was decanted, and the remaining crystalline solid was treated with five soaks in *ca.* 500 mL of DMF, each for 1 h at 130 °C. After cooling to ambient temperature, the solid was then treated with two soaks in *ca.* 250 mL of Ac₂O, each for 12 h, four soaks in *ca.* 300 mL of CH₂Cl₂, each for 1 h, and four soaks in *ca.* 300 mL of Et₂O, each for 1 h. The solid was dried for 12 h at 150 °C under high vacuum to yield **1** as a purple crystalline solid. Yield = 1.42 g (45.2%). Subsequent manipulations of this compound were carried out in a solvent-free glovebox. Anal. Calcd. for C₁₆₈H₁₂₂N₁₂O₆₄Zr₁₂ (**1**): C, 45.58; H, 2.78; N, 3.80. Found: C, 46.78; H, 2.45; N, 4.48. UV-vis (diffuse reflectance, nm): 303, 428, 526, 563, 593, 649. Experimental Brunauer-Emmett-Teller (BET) surface area: 3586(15) m²/g.

(H₂TCPP)₃{Zr₆O₄(μ-OH)₄(OH)₆}₂, PCN-224 (2). This preparation was performed under air. In a 20-mL scintillation vial, the compound **1** (229 mg, 51.7 μmol) was treated with five soaks in *ca.* 20 mL of methanol, each for 1 h at 60 °C. The mixture was cooled to room temperature, then the solid was soaked twice in *ca.* 20 mL solution of water in acetone (10% v/v), each for 12 h, four times in *ca.* 20 mL of acetone, each for 1 h, four times in *ca.* 20 mL of CH₂Cl₂, each for 1 h, and four times in *ca.* 20 mL of Et₂O, each for 1 h. The solid was dried for 12 h at 150 °C under high vacuum to yield **2** as a purple crystalline solid. Yield = 200 mg (92.3%). Subsequent manipulations of this compound were carried out in a solvent-free glovebox. Anal. Calcd. for C₁₄₄H₉₈N₁₂O₅₂Zr₁₂ (**2**): C, 44.49; H, 2.52; N, 4.28. Found: C, 45.72; H, 2.52; N, 4.67. UV-vis (diffuse reflectance, nm): 304, 423, 526, 564, 595, 654. Experimental BET surface area: 3638(16) m²/g.

{Fe(Cl)(TCPP)}₃{Zr₆O₄(OH)₄(CH₃CO₂)₆}₂, PCN-224'FeCl (1FeCl). The compounds **1** (500 mg, 113 μmol), FeCl₃ (276 mg, 1.70 mmol), 2,6-lutidine (364 mg, 3.40 mmol), and DMF (17.0 mL) were added to a 20-mL scintillation vial to give a yellow-orange solution with the crystalline purple solid. The vial was sealed with a Teflon-lined cap, then heated at 100 °C for 12 h. Afterwards, the solution was decanted, and the solid was soaked ten times in *ca.* 20 mL of DMF, each for 1 h at 100 °C. After cooling to ambient temperature, the solid was then treated with two soaks in *ca.* 20 mL of Ac₂O, each for 12 h, four soaks in *ca.* 20 mL of CH₂Cl₂, each for 1 h, and four soaks in *ca.* 20 mL of Et₂O, each for 1 h. The solid was dried for 12 h at 150 °C under high vacuum to yield **1FeCl** as a purple crystalline solid. Yield = 470 mg (88.7%). Subsequent manipulations of this compound were carried out in a solvent-free glovebox. Anal. Calcd. for C₁₆₈H₁₁₆Cl₃Fe₃N₁₂O₆₄Zr₁₂ (**1FeCl**): C, 42.98; H, 2.49; N, 3.58. Found: C, 41.55; H, 2.37; N, 4.46. Expected Zr to Fe mole ratio: 4.0. Found: 4.9(1). UV-vis (diffuse reflectance, nm): 432, 518, 694. Experimental BET surface area: 3011(9) m²/g.

{Fe(Cl)(TCPP)}₃{Zr₆O₄(μ-OH)₄(OH)₆}₂, PCN-224FeCl (2FeCl). In a 20-mL scintillation vial, the compound **1FeCl** (350 mg, 79.1 μmol) treated in four soaks of methanol, each for 1 h at 60 °C. The vial was then allowed to cool to ambient temperature and removed from the glovebox. The solution was decanted, and the solid was soaked twice in *ca.* 20 mL solution of water in acetone (10% v/v), each for 12 h, four times in *ca.* 20 mL of acetone, each for 1 h, four times in *ca.* 20 mL of CH₂Cl₂, each for 1 h, and four times in *ca.* 20 mL of Et₂O, each for 1 h. The solid was dried for 12 h at 150 °C under high vacuum to yield **2FeCl** as a purple crystalline solid. Yield = 272 mg (82.2%). Subsequent manipulations of this compound were carried out in a solvent-free glovebox. Anal. Calcd. for C₁₄₄H₉₂Cl₃Fe₃N₁₂O₅₂Zr₁₂ (**2FeCl**): C, 41.27; H, 2.21; N, 4.01. Found: C, 41.41; H, 2.33; N, 4.27. Expected Zr to Fe mole ratio: 4.0. Found: 4.6(1). UV-vis (diffuse reflectance, nm): 431, 521, 694. Experimental BET surface area: 3204(9) m²/g.

Single Crystals of PCN-224' (1). This preparation was performed under air. Also, this preparation afforded larger single crystals using the vials described below than in other sealed tubes or reaction vessels. In a 22-mL glass sample vial with a Teflon-lined cap (Qorpak, Item# GLC-01002), a mixture of zirconium tetrachloride (45 mg, 0.19 mmol) and DMF (3.0 mL) were sonicated for 1 h to give a clear, colorless solution. Benzoic acid (0.81 g, 6.6 mmol) and acetic acid (2.7 g, 46 mmol) were then added, and the mixture was sonicated for 1 h to give a colorless solution. The compound H₆TCPP (15 mg, 19 μmol) was added, and the mixture was sonicated for 1 h to give a green solution. The mixture was sealed and heated to 130 °C for 10 d in an oven to give purple crystals in a dark brown solution. The crystals were soaked five times in *ca.* 20 mL of DMF at 130 °C, then allowed to cool to ambient temperature. The crystals were treated with two soaks in *ca.* 10 mL of Ac₂O at ambient temperature, each for 12 h, four soaks of *ca.* 20 mL of CH₂Cl₂, each for 1 h, and four soaks in *ca.* 20 mL of Et₂O, each for 1 h. The crystals were dried

for 12 h at 150 °C under high vacuum to yield cuboctahedron-shaped crystals of **1** suitable for single-crystal X-ray diffraction analysis.

Single Crystals of PCN-224 (2). This preparation was performed under air. In a 4-mL scintillation vial, single crystals of **1** were treated with five soaks in *ca.* 4 mL of methanol, each for 1 h at 60 °C. The mixture was cooled to room temperature, then the solid was soaked twice in *ca.* 4 mL solution of water in acetone (10% v/v), each for 12 h, four times in *ca.* 4 mL of acetone, each for 1 h, four times in *ca.* 4 mL of CH₂Cl₂, each for 1 h, and four times in *ca.* 4 mL of Et₂O, each for 1 h. The purple cuboctahedron-shaped crystals were dried for 12 h at 150 °C under high vacuum to yield cuboctahedron-shaped crystals of **2** suitable for single-crystal X-ray diffraction analysis.

Single Crystals of PCN-224'FeCl (1FeCl). In a 4-mL scintillation vial, single crystals of **1** (10 mg, 2.3 μmol) were soaked twice in *ca.* 4 mL of anhydrous THF, each for 30 mins, then soaked twice in anhydrous DMF, each for 30 mins. The DMF solution was removed with a pipette, then a solution of FeCl₃ (8.1 mg, 50 μmol) and 2,6-lutidine (0.10 mmol) dissolved in 0.50 mL of DMF was added. The vial was sealed with a Teflon-lined cap and heated at 100 °C for 12 h. Afterwards, the solution was decanted. The crystals were soaked five times in *ca.* 4 mL of DMF, each for 1 h at 100 °C. After cooling to ambient temperature, the crystals were soaked twice in *ca.* 4 mL of Ac₂O, each for 12 h, four soaks in *ca.* 4 mL of CH₂Cl₂, each for 1 h, and four soaks in *ca.* 4 mL of Et₂O, each for 1 h. The crystals were dried for 12 h at 150 °C under high vacuum to afford cuboctahedron-shaped crystals of **1FeCl** that were characterized with single-crystal X-ray diffraction analysis.

Powder X-ray Diffraction (PXRD) Analyses. In a solvent-free glovebox, activated powder samples of **1**, **2**, **1FeCl**, and **2FeCl** were packed into metallic sample holders with 3 mm diameter apertures and sandwiched between two layers of polyimide tape. Diffractograms were collected at ambient temperature on a STOE STADI-P powder diffractometer equipped with an asymmetric curved Ge monochromator (Cu-Kα₁ radiation, λ = 1.54056 Å) and a one-dimensional Si strip detector (MYTHEN2 1K from DECTRIS). The line-focused Cu X-ray tube was operated at 40 kV and 40 mA. The measurement was performed with a transmission geometry, with the detector moved at 2θ steps of 1°. Intensity data of 2θ = 2–60° were collected over a period of 30 min. The instrument was calibrated against a NIST Si standard (640d) prior to measurement.

X-ray Structure Determination. In a solvent-free, N₂-filled glovebox, activated crystals of **1**, **2**, and **1FeCl** were coated with Paratone-N oil prior to removal from the glovebox. The crystals were mounted on MiTeGen loops and were each cooled under a stream of N₂ (100 K; Oxford Cryostream 700) during measurements. Data were collected using a Bruker APEX II QUAZAR diffractometer equipped with a Microfocus Sealed Source (Incoatec IμS; Mo-Kα λ = 0.71073 Å or Cu-Kα λ = 1.54056 Å). Raw data were integrated and corrected for Lorentz and polarization effects using APEX3.⁷ Absorption corrections were applied using SADABS.⁸ Space group assignments were determined by examination of systematic absences, *E*-statistics, and successive refinement of the structures. Structures were solved using SHELXS⁹ and all non-hydrogen atoms were refined anisotropically by full-matrix least-squares (SHELXL)¹⁰ in conjunction with the OLEX2 software.¹¹ Carbon-bound hydrogen atoms were inserted at idealized positions and refined isotropically using the appropriate HFIX command in SHELXL. Solvent masking was not necessary for the refinements of **1** and **1FeCl**; a solvent mask was needed for **2** to address residual electron density within the pores not accounted by the model (see Table S3 for refinement parameters before and after the solvent mask).

Disorder was addressed using the following constraints and restraints. The RIGU restraints were applied separately to the zirconium-oxo clusters and porphyrin/heme linkers. The SIMU restraints were applied to the entire structures of **1**, **2**, and **1FeCl**. The bridging oxygen atoms O2 and O2A were refined to two positions at occupancies of 51(4):49(4) for **1** and 56(5):44(5) for **1FeCl** (see Figure S10); this disorder likely reflects the bridging oxo versus hydroxo ligands in the $[\text{Zr}_6\text{O}_4(\text{OH})_4]^{12+}$ clusters. The acetate ligands in **1** and **1FeCl** were disordered over two positions, either bridging two Zr atoms, or binding one Zr atom as a bidentate ligand. The occupancies of the acetate ligands over these two positions were refined to 75(2):25(2) in **1** and 61(3):39(3) in **1FeCl**. The SADI and FLAT restraints were also applied to the acetate ligands to ensure they refined stably and with the appropriate geometry. In the case of **1FeCl**, the acetate methyl carbon atom C10 exhibited a large, prolate-shaped thermal ellipsoid ($U_{\text{eq}} > 1$), consistent the acetate ligand showing a “wagging” motion. Since the C10 atom corresponds to only 75% of an acetate methyl group, the residual electron density was not sufficiently resolved to model the disorder. Thus, the wagging disorder was not modeled, and the ISOR restraint ($\text{st} = 0.2$) was applied to C10.

Mössbauer Spectroscopy. Zero-field ^{57}Fe Mössbauer spectra were obtained at 80 K with a constant acceleration spectrometer with a rhodium matrix cobalt-57 source. Prior to measurements, the spectrometer was calibrated at 295 K with a 30 μm -thick α -iron foil. Absorbers were prepared under a dinitrogen atmosphere by placing 100–130 mg of compound **1FeCl** or **2FeCl**, or 40 mg of (TPP)FeCl into a polyethylene holder (3–4 mg of natural Fe/ cm^2) and restrained with one to two drops of Paratone-N oil. The absorbers were frozen in liquid nitrogen immediately upon removal from the glovebox. Collected spectra were analyzed using the WMOSS software package.¹² Isomer shifts are reported relative to the centroid of the iron metal spectrum recorded at 295 K.

Diffuse Reflectance Infrared Fourier Transform Spectroscopy (DRIFTS). In a solvent-free glovebox, samples of **1**, **2**, **1FeCl**, and **2FeCl** were prepared as *ca.* 20 wt% dilutions in KBr (MilliporeSigma, BioUltra, $\geq 99.5\%$, dried under high vacuum at 150 °C for 12 h) and pulverized in a mortar and pestle to give homogeneous powders. The samples were then transferred to a Harrick Praying Mantis™ High Temperature Reaction Chamber equipped with CaF_2 windows, sealed, and attached to a Harrick Praying Mantis™ Diffuse Reflection accessory to perform DRIFTS measurements. Measurements were performed on a Thermo Nicolet 6700 FTIR spectrometer operating at a resolution of 4 cm^{-1} . Sample measurements were conducted at ambient temperature under a static atmosphere of N_2 from the glovebox. The data was averaged over 64 scans. The collected data were treated with a background correction of the reaction chamber containing only KBr and are reported as Kubelka-Munk transform. The spectra were normalized using the intensity of a common feature at *ca.* 3130 cm^{-1} against the baseline absorption at 4000 cm^{-1} .

Diffuse Reflectance UV-Visible Spectroscopy. In a solvent-free glovebox, samples of TPP, (TPP)FeCl, **1**, **2**, **1FeCl**, and **2FeCl** were prepared as *ca.* 5 wt% dilutions in BaSO_4 (Honeywell, 99%, dried under high vacuum at 150 °C for 12 h) and pulverized in a mortar and pestle to give homogeneous purple (for TPP, **1**, and **2**) or brown (for (TPP)FeCl, **1FeCl**, and **2FeCl**) powders. The samples were then transferred to a Harrick Praying Mantis™ Ambient Chamber equipped with quartz windows, sealed, and attached to a Harrick Praying Mantis™ Diffuse Reflection accessory to perform UV-vis measurements. Measurements were performed on an Agilent Cary 5000 spectrophotometer. Sample measurements were conducted at ambient temperature under a static atmosphere of N_2 from the glovebox. The collected data were treated with a background

correction of the sample chamber containing only BaSO₄ and are reported as Kubelka-Munk transform.

Framework Digestion and ¹H NMR Analysis Protocol. First, 2–4 mg of activated **1** or **2** were each placed into a 20 mL scintillation vial. Then, under air, 70 μL of D₂SO₄ (Cambridge Isotope Laboratories, 99% D, 96–98% in D₂O) and 630 μL of dimethyl sulfoxide-d₆ (Cambridge Isotope Laboratories, 99.9% D) were added to each vial. The vials were capped, then sonicated for 15 min at ambient temperature to afford a homogeneous, dark green solution. The solutions were then transferred into NMR tubes, and ¹H NMR spectra were acquired using a Bruker Avance III 500 MHz HD spectrometer equipped with a TXO Prodigy probe. NMR spectra were referenced relative to tetramethylsilane using the residual dimethyl sulfoxide-d₅ signal (δ = 2.50). The ratio of [H₂TCPP]⁴⁻ versus [CH₃CO₂]⁻ was quantified by the relative areas of the ¹H peaks for [H₈TCPP]²⁺ (δ 8.76 (d, *J* = 7.9 Hz, 8 phenyl ArH per porphyrin), 8.73 (s, 8 porphyrin ArH per porphyrin), 8.54 (d, *J* = 7.9 Hz, 8 phenyl ArH per porphyrin)), and those of CH₃CO₂H (δ 1.81 (s, CH₃)).

Elemental Analyses. Quantification of C, H, and N was accomplished using combustion analysis at the Integrated Molecular Structure Education and Research Center at Northwestern University. Each combustion analysis was performed in triplicate: the average C, H, and N values are reported.

Quantification of Zr and Fe was accomplished using inductively coupled plasma-optical emission spectroscopy (ICP-OES) of acid digested samples. Specifically, samples of **1FeCl** and **2FeCl** (ranging from 1–3 mg) were each digested in a 50 mL metal-free centrifuge tube with 5000 μL of 4.8 wt% hydrofluoric acid (prepared by dilution of 48 wt% HF, MilliporeSigma, ≥99.99% metals basis), 4000 μL of concentrated nitric acid (Fisher Chemical, TraceMetal™ grade), 500 μL of concentrated HCl (Fisher Chemical, TraceMetal™ grade), and 500 μL of H₂O₂ (30% solution in water, MilliporeSigma, for trace analysis), and heated at 65 °C for 48 h to allow for complete sample digestion. A 1000 μL aliquot of each digestate was diluted with ultra-pure H₂O (18.2 MΩ·cm) to produce a final solution of 4.0% nitric acid in a total sample volume of 10 mL. Quantitative standards of Zr and Fe consisting of 20.0, 10.0, 5.00, 2.50, 1.25, and 0.625 ppm were made using 1000 ppm Zr and 100 ppm Fe standards (Inorganic Ventures) in 4.0% nitric acid. ICP-OES measurements were performed using a Thermo Scientific iCap7600 instrument operating in radial view. Each sample was acquired using a 5 second visible exposure time and a 15 second UV exposure time, running three replicates. The spectral lines selected for analysis were: Zr (327.305, 339.198, and 343.823 nm) and Fe (238.204 and 259.940 nm). The concentrations obtained across the three replicates and using the different spectral lines were used to calculate the standard deviations of Zr to Fe mole ratios.

Surface Area Characterization. In a solvent-free glovebox activated samples of ~40 mg **1**, **2**, **1FeCl**, and **2FeCl** were each transferred to pre-weighed analysis tubes, which were stoppered with a check seal. Samples were further degassed on a Micromeritics Smart VacPrep system equipped with a turbomolecular pump. Samples were degassed at 150 °C for 24 h, after which the outgas rates were less than 2.5 mTorr/min. Surface area analyses were then conducted on a Micromeritics 3Flex instrument with UHP-grade (99.999% purity) N₂. The N₂ isotherms at 77 K were measured in a liquid nitrogen bath. The void volumes (also called free spaces or dead spaces) of all samples were determined with UHP He after the N₂ isotherm measurements.¹³ The Brunauer-Emmett-Teller (BET) surface areas of **1**, **2**, **1FeCl**, and **2FeCl** were calculated from the 77 K N₂ isotherms using the BET equation¹⁴ and a cross-sectional area of 0.162 nm² for N₂¹³:

$$\frac{p/p^\circ}{n(1 - p/p^\circ)} = \frac{1}{n_m C} + \frac{C - 1}{n_m C} \left(\frac{p}{p^\circ} \right) \quad (1)$$

where n is the amount adsorbed at relative pressure p/p° , n_m is the monolayer capacity, and C is a parameter exponentially related to the energy of monolayer adsorption. The ranges of p/p° selected for eq. 1 satisfied the following four consistency criteria^{14a} (see Figures S13–16 and Table S5):

1. the value C is positive;
2. the term $n(1 - p/p^\circ)$ increases monotonically with p/p° ;
3. the relative pressure at monolayer capacity, $[p/p^\circ]n_m$, is within the pressure range selected for the BET calculation;
4. the value $1/(\sqrt{C} + 1)$ is within 10% of $[p/p^\circ]n_m$.

Calculated Surface Areas. The N₂ accessible surface areas of frameworks **1**, **2**, and **1FeCl** were calculated from their respective X-ray crystal structures using the Zeo++ software¹⁵ and the probe-accessible surface area methodology outlined by Smit and coworkers.¹⁶ Specifically, we chose a probe radius of 1.86 Å corresponding to N₂.¹⁶⁻¹⁷ Table S6 shows the volumetric probe-accessible surface areas estimated by Zeo++, which were converted to gravimetric surface areas by dividing with the crystallographic densities of each framework.

Catalytic Cyclohexane Hydroxylation Protocol with Iodosylbenzene. In a 20-mL scintillation vial equipped with a Teflon-coated stir bar and a Teflon-lined screw cap, a 10 μmol portion of Fe catalyst (i.e. 3.3 μmol of **1FeCl** or **2FeCl**) was suspended (or dissolved in the case of (TPP)FeCl and FeCl₃) into 2000 μL of a 2.0 M solution of cyclohexane (4.0 mmol) in dichloromethane. In the control experiments with methanol, acetic acid, or tetrabutyl ammonium acetate, the additive was added at this stage. The mixture was stirred vigorously at 1500 rpm for 30 min at 30 °C to ensure the substrate and solvent had fully penetrated into the framework. Iodosylbenzene (44 mg, 0.20 mmol) was added to the vial in one portion, and the reaction was sealed and allowed to stir at 1500 rpm for 6 h at 30 °C. After this time, a 20 μL aliquot of the reaction solution was diluted with 480 μL of CH₂Cl₂. The solution was filtered through a PTFE membrane filter with a pore size of 0.2 μm, then analyzed for cyclohexanol, cyclohexanone, and chlorocyclohexane by gas chromatography–mass spectrometry (GCMS).

GCMS analysis was performed using an Agilent 5973 GCMS equipped with a DB-5 column. Quantification of cyclohexanol, cyclohexanone, and chlorocyclohexane was performed using their extracted ion chromatograms (cyclohexanol, m/z = 57; cyclohexanone, m/z = 98; and chlorocyclohexane, m/z = 67) and external calibration against dichloromethane solutions containing cyclohexanol, cyclohexanone, and chlorocyclohexane of concentrations 0.25–100 mM. Each catalysis condition was performed in triplicate. The average yield is reported, and the standard deviation across the three runs is reported in parentheses.

Catalytic Cyclohexane Hydroxylation Protocol with 2-*tert*-butylsulfonyliodosylbenzene. These experiments were performed and analyzed in the same manner as the experiments using iodosylbenzene (see above), except the 2-*tert*-butylsulfonyliodosylbenzene (68 mg, 0.20 mmol) was added in four portions over 30 min, and the reaction was allowed to stir for 24 h instead. No replicates were performed.

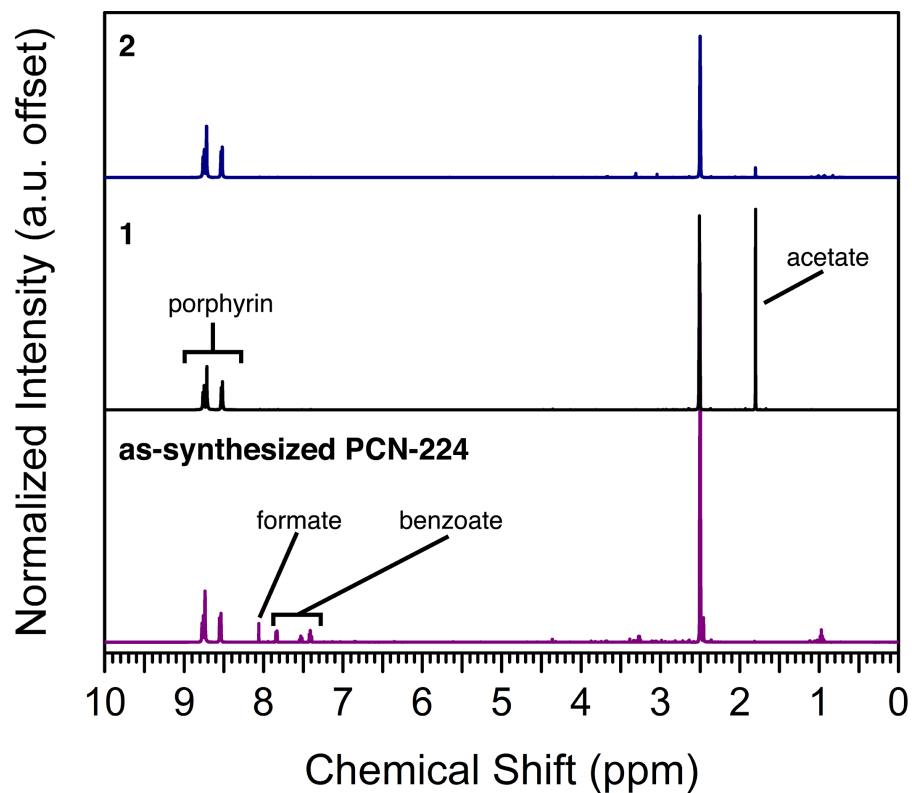


Figure S1. The ^1H NMR spectra of as-synthesized PCN-224 (purple), **1** (black), and **2** (blue) digested in $\text{D}_2\text{SO}_4/\text{DMSO-}d_6$. The spectra are normalized to the intensities of the $[\text{H}_6\text{TCPP}]^{2+}$ resonances between 8.5 to 9 ppm. The peaks between 7.3 and 8.1 ppm are due to formate and benzoate ligands present in as-synthesized PCN-224. The peaks at 1.81 ppm are due to acetate ligands in **1** and **2**. The peaks at 2.50 ppm are due to $\text{DMSO-}d_5$. The peaks between 12 to 13 ppm due to H_3O^+ are not shown.

Table S1. Quantification of $[\text{H}_2\text{TCPP}]^{4-}$ to acetate, formate, and benzoate in digestates of MOFs by ^1H NMR.

compound	porphyrin : acetate mole ratio	notes
as-synthesized PCN-224	no acetate detected	In addition, 2.3 equivalents of formate and 3.0 equivalents of benzoate detected per 3.0 moles of $[\text{H}_2\text{TCPP}]^{4-}$.
1	3 : 9.3	The porphyrin : acetate mole ratio deviates from the expected 3 : 12 ratio in the idealized formula $[\text{H}_2\text{TCPP}]_3[\text{Zr}_6\text{O}_4(\text{OH})_4(\text{CH}_3\text{CO}_2)_6]_2$. We attribute this difference to either non-periodic replacement of non-structural, monotopic ligands with $\text{H}_2\text{TCPP}^{4-}$, or the presence of the morphologically-related framework MOF-525, $[\text{H}_2\text{TCPP}][\text{Zr}_6\text{O}_4(\text{OH})_4]$. ¹⁸
single crystals of 1	3 : 12	The porphyrin : acetate mole ratio is consistent with the idealized formula of $[\text{H}_2\text{TCPP}]_3[\text{Zr}_6\text{O}_4(\text{OH})_4(\text{CH}_3\text{CO}_2)_6]_2$.
2	3 : 0.5	Less than 0.3 equivalents of CH_3OH was detected per 3.0 moles of $[\text{H}_2\text{TCPP}]^{4-}$.

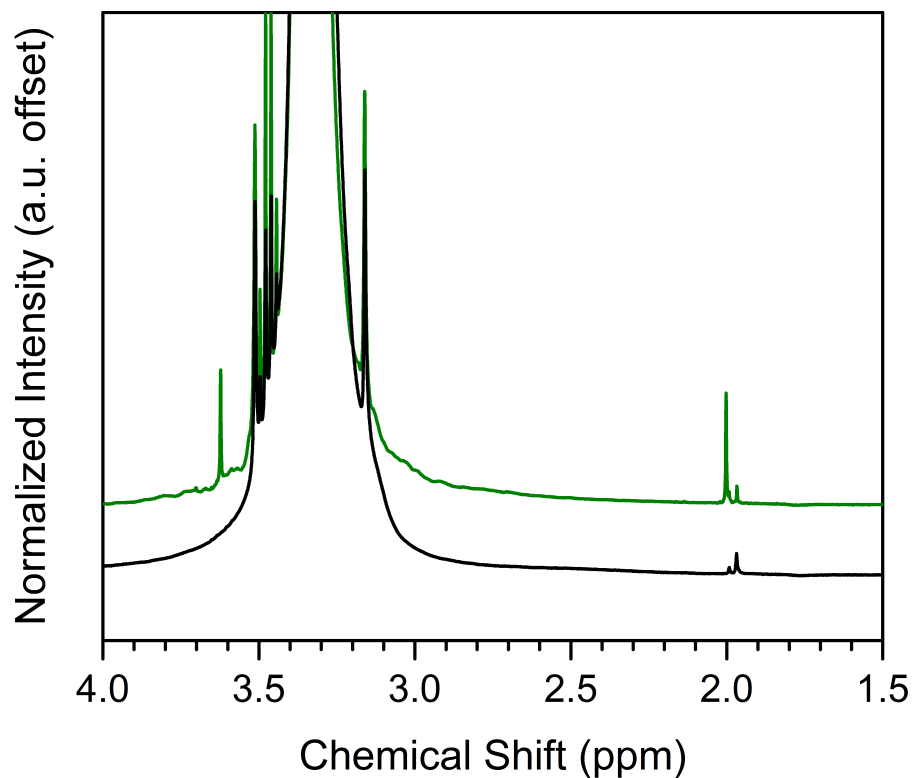


Figure S2. Methyl acetate formation from methanol and **1**. The ¹H NMR spectra of a CH₃OH solution containing **1** before (black trace) and after heating at 60 °C for 1 h (green trace). The two singlets of equal intensity at 3.62 and 2.00 ppm peaks correspond to the formation of methyl acetate (lit. δ 3.64, 2.02 ppm¹⁹) and suggest that the acetylated acetylated Zr₆ nodes in **1** carry out the esterification of methanol.

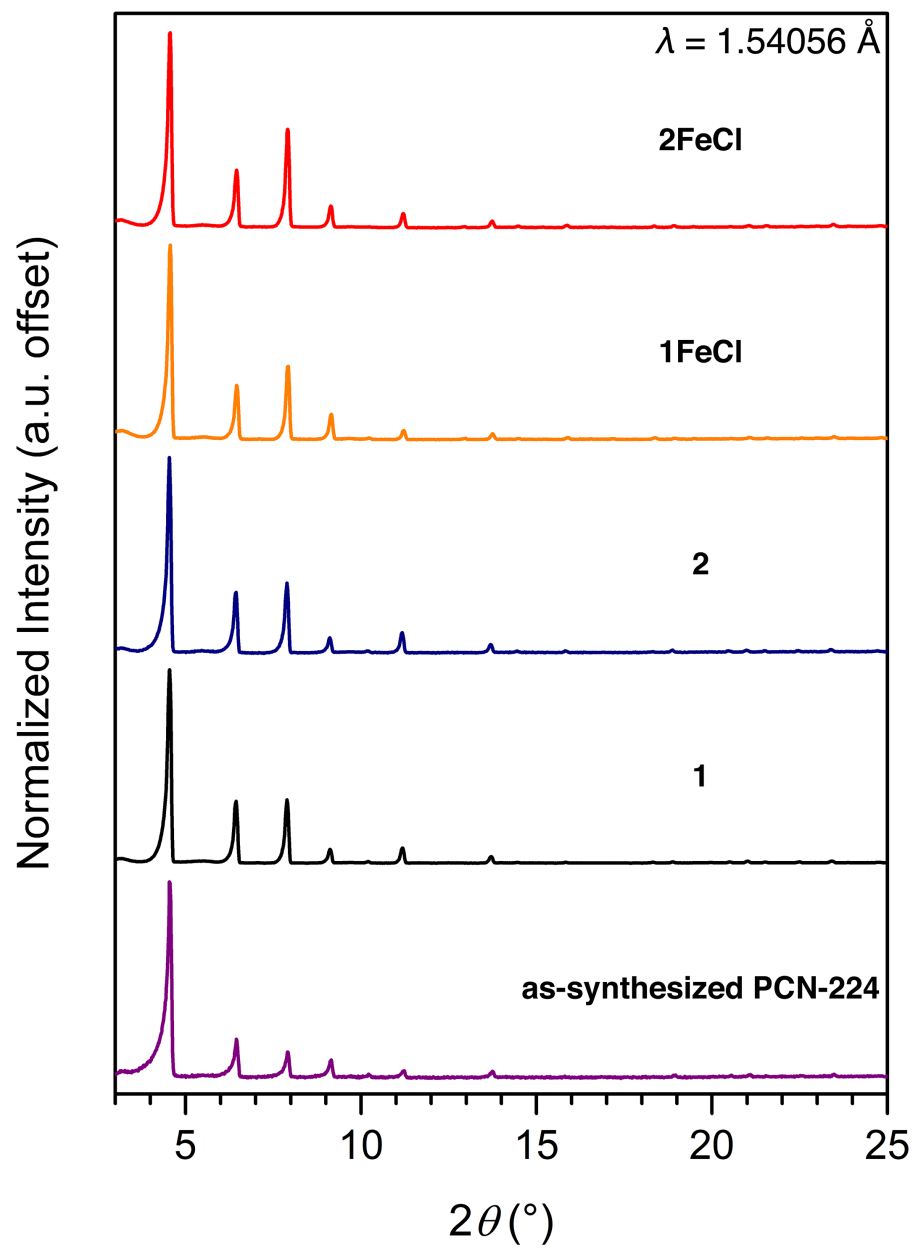


Figure S3. The PXRD patterns of as-synthesized PCN-224 (purple), **1** (black), **2** (blue), **1FeCl** (orange), and **2FeCl** (red).

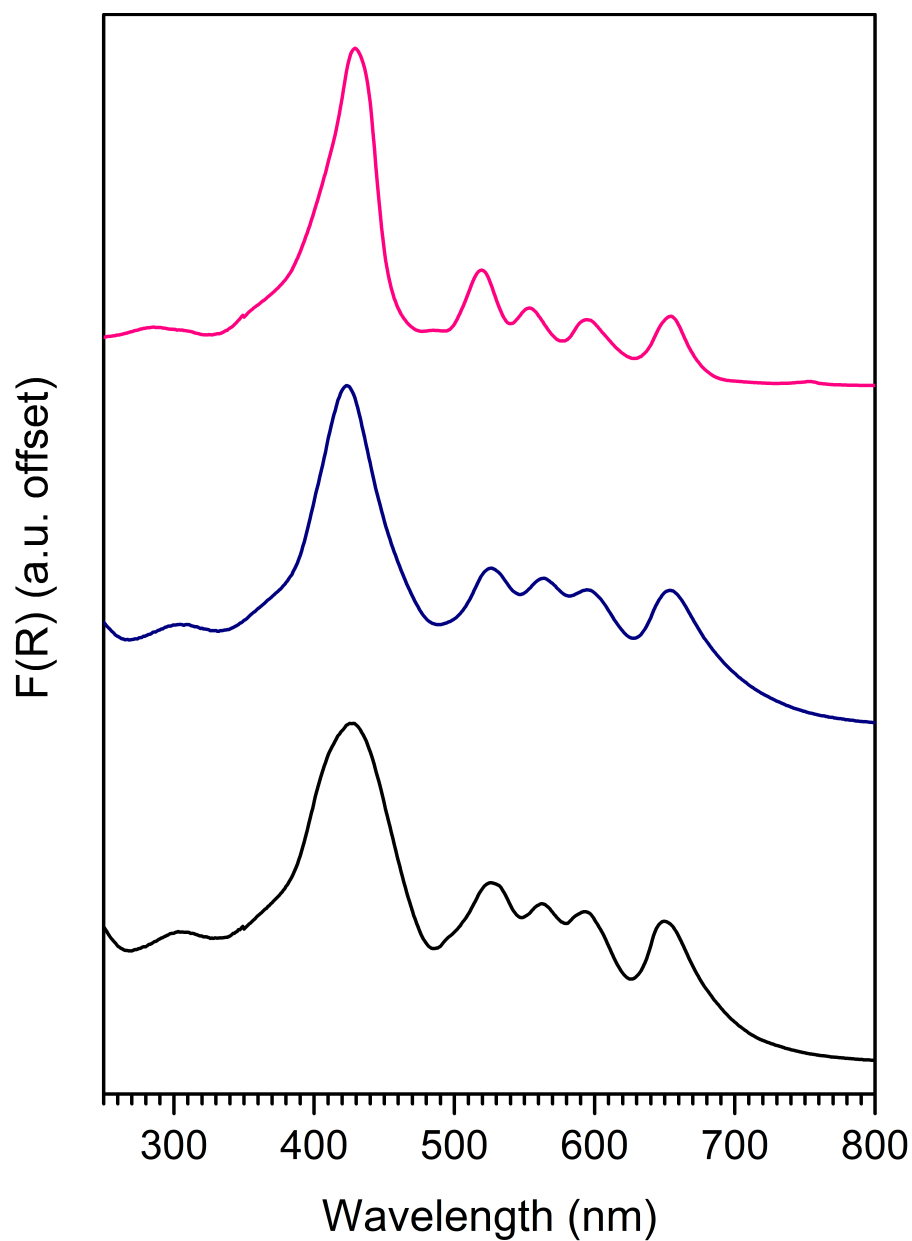


Figure S4. The diffuse reflectance UV-vis spectra of **1** (black), **2** (navy), and tetraphenylporphyrin (pink). The Soret band at 428 nm and the Q bands between 500 to 700 nm are conserved between the spectra of **1** and **2**, indicating that the deacetylation of **1** does not alter the chemical structure of the porphyrin unit. Furthermore, the UV-vis spectra of **1** and **2** show that the electronic structure of their porphyrin linkers are similar to those of the molecular tetraphenylporphyrin.

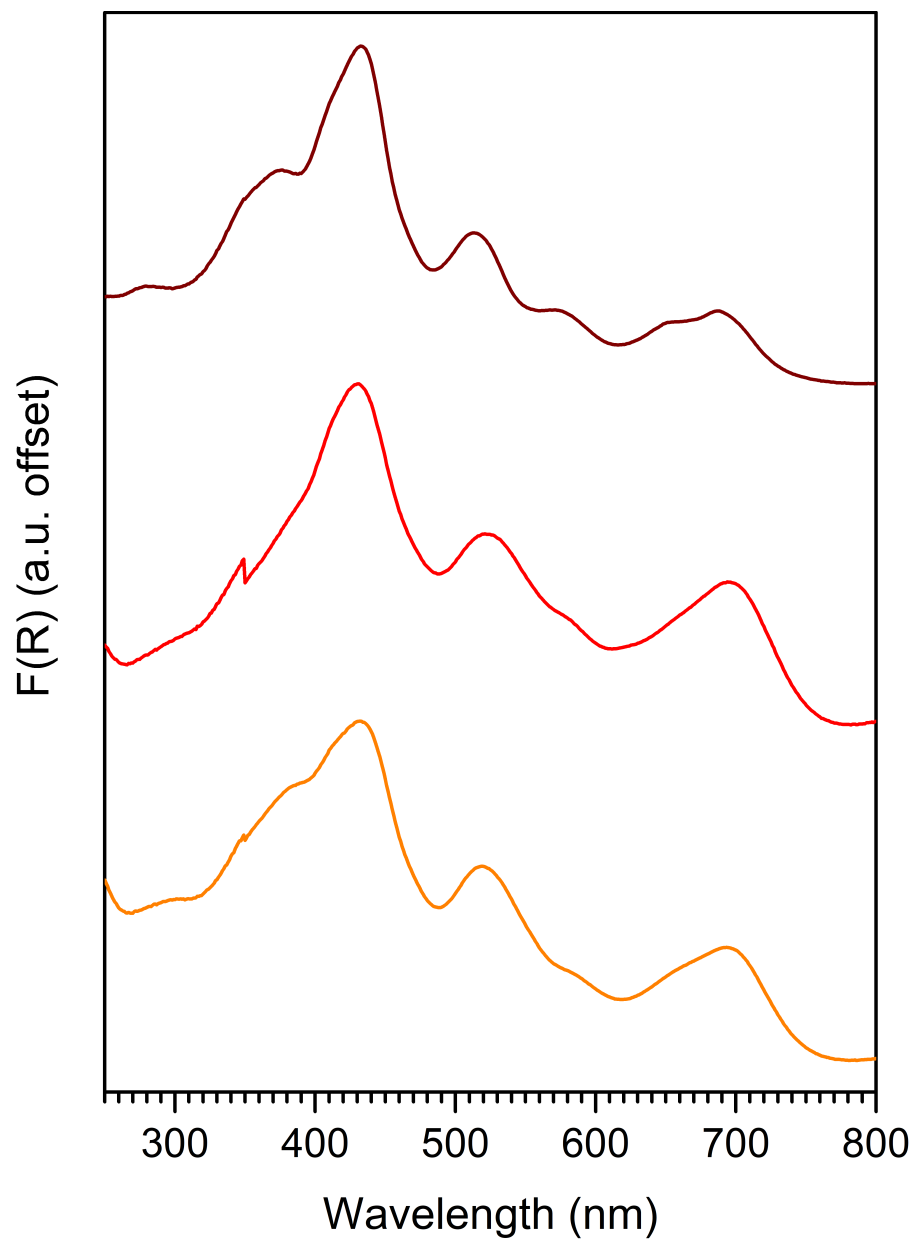


Figure S5. The diffuse reflectance UV-vis spectra of **1FeCl** (orange), **2FeCl** (red), and (TPP)FeCl (brown). Compared with the UV-vis spectra of **1** and **2** (Figure S4), the presence of fewer Q bands between 500 to 700 nm for **1FeCl** and **2FeCl** is consistent with the higher symmetry of the metalated porphyrin as compared to the free base porphyrins in **1** and **2**. The similarity between the spectra of **1FeCl**, **2FeCl**, and (TPP)FeCl indicate that the porphyrin units are metalated by chloride-ligated ferric ions. The discontinuities at 350 nm are spectral artefacts caused by a grating change in the spectrometer.

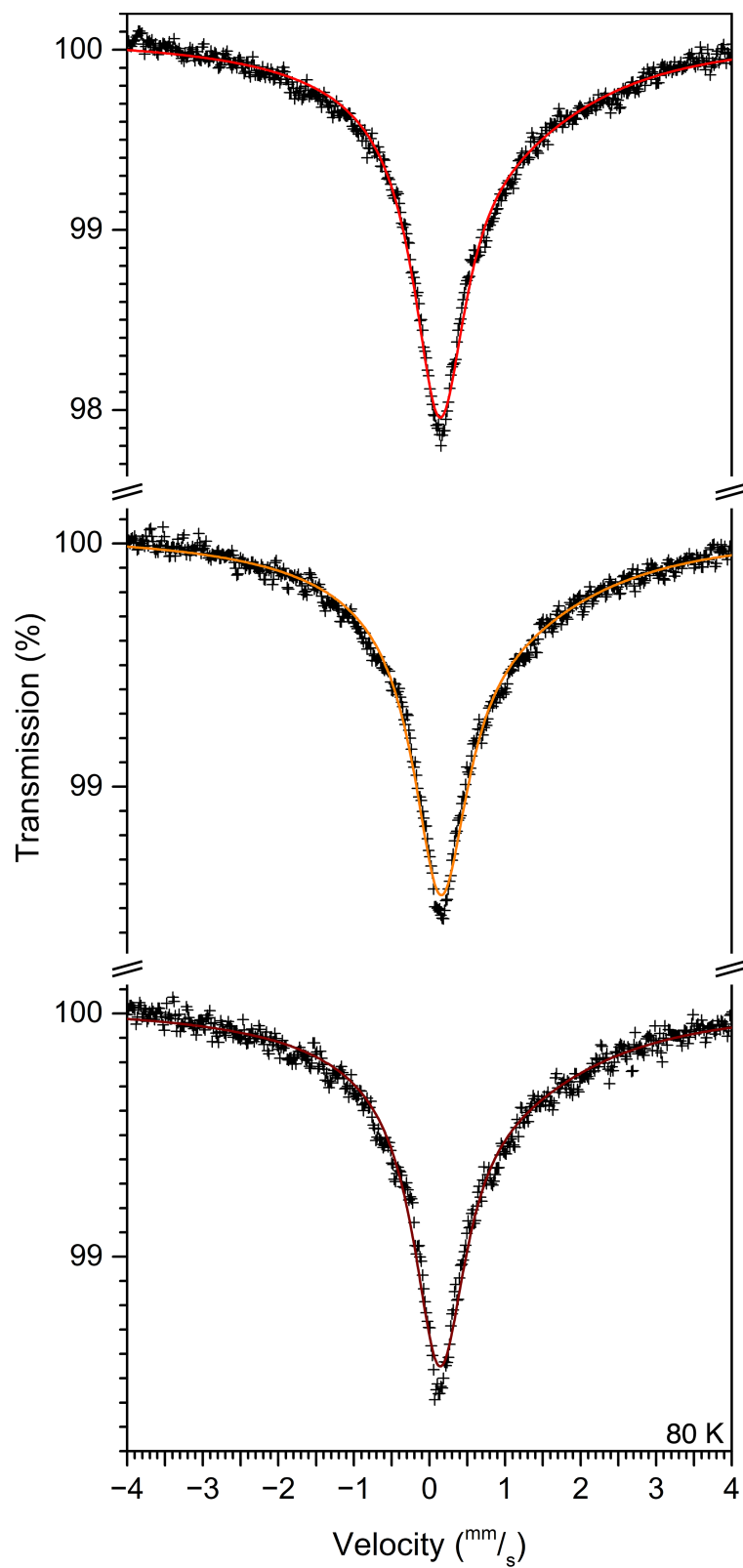


Figure S6. Zero-field ^{57}Fe Mössbauer spectra of (TPP)FeCl (bottom), **1FeCl** (middle), and **2FeCl** (top) at 80 K. Black crosses represent experimental data and colored lines represent fits. Fit parameters are shown in Table S2.

Table S2. Fit parameters for the zero-field ^{57}Fe Mössbauer spectra of (TPP)FeCl and frameworks **1FeCl** and **2FeCl**.

compound	δ (mm/s)	$ \Delta E_Q $ (mm/s)	Γ_L (mm/s)	Γ_R (mm/s)
(TPP)FeCl	0.40(2)	0.54(4)	0.84(2)	3.6(3)
1FeCl	0.40(2)	0.50(3)	0.87(2)	3.6(2)
2FeCl	0.44(2)	0.60(3)	0.84(2)	3.4(2)

Table S3. Crystallographic details for frameworks **1**, **1FeCl**, and **2**.

	1	1FeCl	2
formula	C ₁₆₈ H ₁₁₄ N ₁₂ O ₆₄ Zr ₁₂	C ₁₆₈ H ₁₀₈ Cl ₃ Fe ₃ N ₁₂ O ₆₄ Zr ₁₂	C ₁₄₄ H ₉₀ N ₁₂ O ₅₂ Zr ₁₂
crystal system	cubic	cubic	cubic
fw, g mol ⁻¹	4419.35	4687.20	3914.91
<i>T</i> , K	100(2)	100(2)	100(2)
λ , Å	1.54056 Å	1.54056 Å	0.71073
space group	<i>Im</i> $\bar{3}m$	<i>Im</i> $\bar{3}m$	<i>Im</i> $\bar{3}m$
habit	block	block	block
color	dark violet	dark violet	dark violet
<i>Z</i> (<i>Z'</i>)	4 (0.041667)	4 (0.041667)	4 (0.041667)
<i>a</i> , Å	38.649(4)	38.4891(9)	38.8372(12)
<i>b</i> , Å	38.649(4)	38.4891(9)	38.8372(12)
<i>c</i> , Å	38.649(4)	38.4891(9)	38.8372(12)
α , °	90	90	90
β , °	90	90	90
γ , °	90	90	90
<i>V</i> , Å ³	55731(19)	57018(4)	58579(5)
ρ_{calc} , g cm ⁻³	0.508	0.546	0.444
μ_{calc} , mm ⁻¹	1.942	2.687	0.227
2 θ range, °	3.232 to 133.132	6.496 to 127.664	1.482 to 58.256
total reflections	240644	167151	370650
data / restr / parameters	4768 / 217 / 139	4419 / 128 / 145	7260 / 80 / 94
<i>F</i> (000)	8792	9284	7736
<i>T</i> _{min} / <i>T</i> _{max}	0.920	0.873	0.931
crystal size, mm ³	0.34 × 0.30 × 0.26	0.25 × 0.24 × 0.22	0.71 × 0.60 × 0.52
Largest diff. peak/hole / e Å ⁻³	1.25 / -0.57	0.93 / -0.35	1.80 / -1.54
<i>R</i> ₁ (<i>wR</i> ₂), % [<i>I</i> > 2 σ (<i>I</i>)]	5.63 (13.99)	7.43 (23.02)	6.96 (20.05)
<i>R</i> ₁ (<i>wR</i> ₂), % (all data)	6.10 (14.50)	8.54 (25.08)	8.45 (22.46)
Solvent mask volume, Å ³ (e ⁻ removed) per asymmetric unit	A solvent mask was not applied.	A solvent mask was not applied.	507 (97)
<i>R</i> ₁ (<i>wR</i> ₂), % (all data, without mask)			17.66 (51.16)

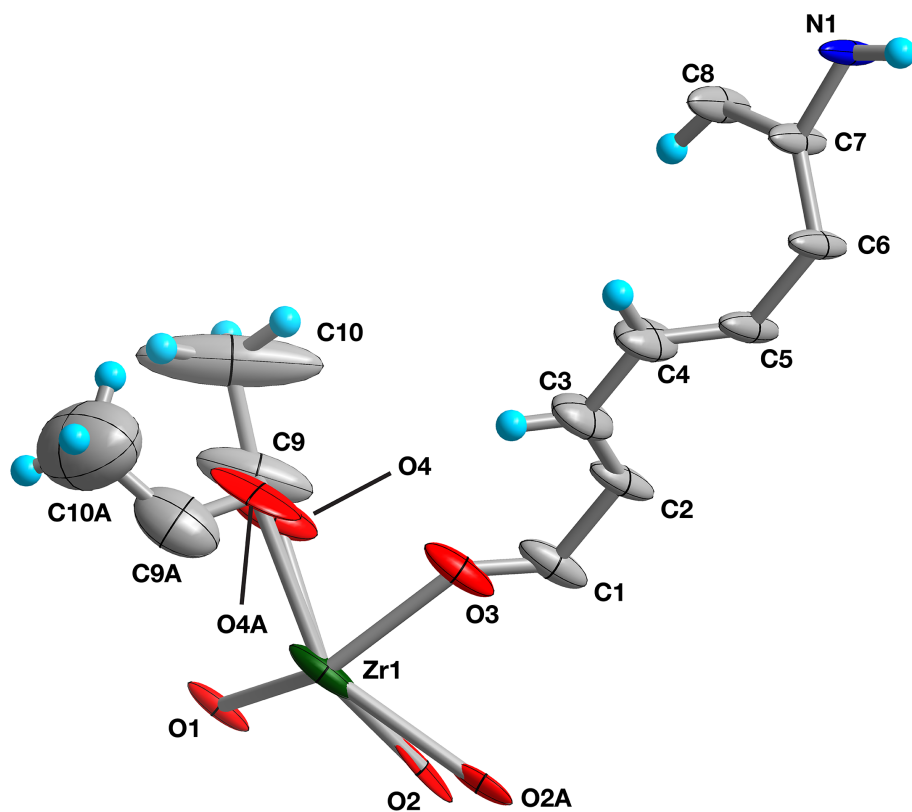


Figure S7. Thermal ellipsoid plot of the single-crystal X-ray structure of **1**. Only the asymmetric unit is depicted. Ellipsoids are drawn at the 50% probability level.

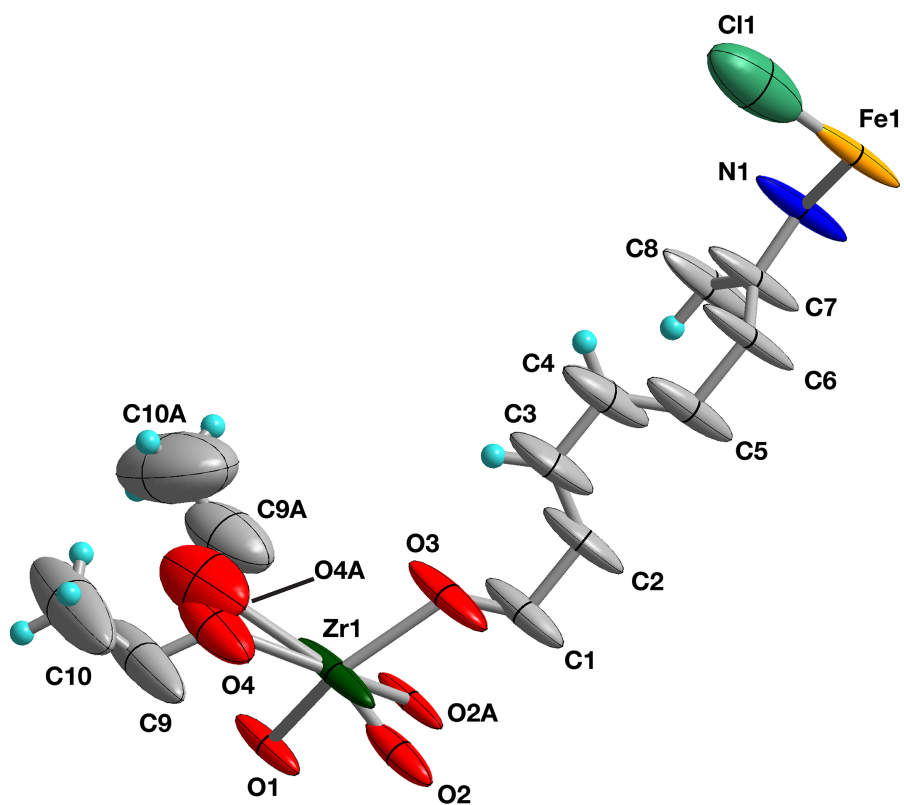


Figure S8. Thermal ellipsoid plot of the single-crystal X-ray structure of **1FeCl**. Only the asymmetric unit is depicted. Ellipsoids are drawn at the 50% probability level.

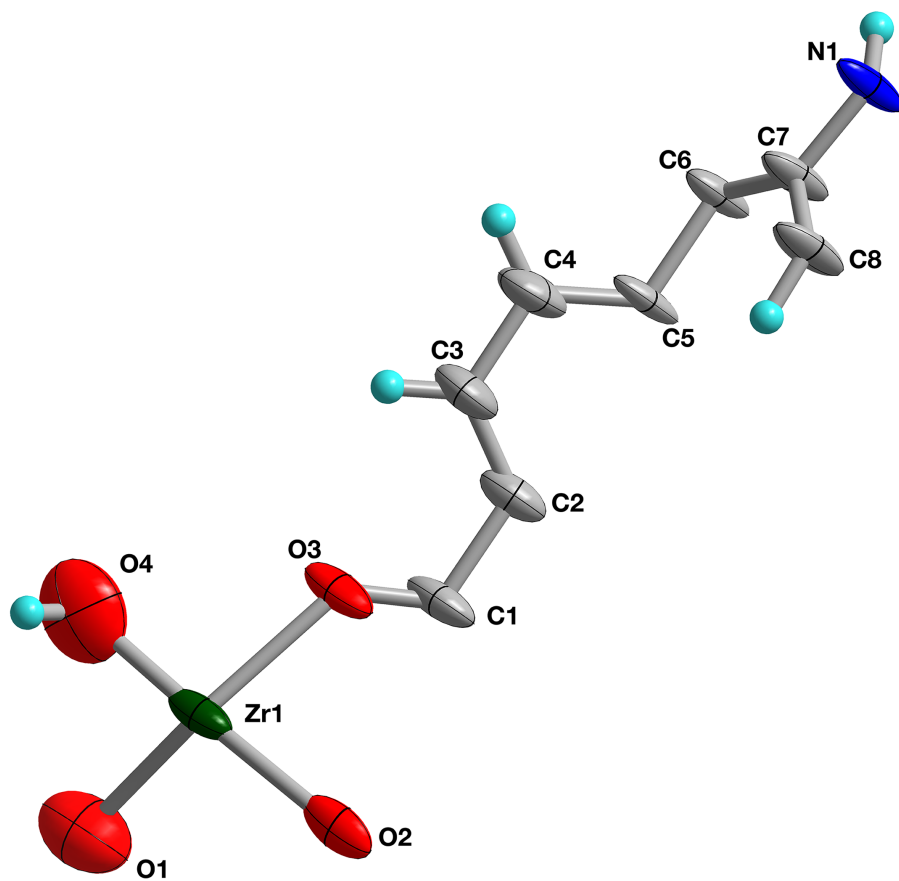


Figure S9. Thermal ellipsoid plot of the single-crystal X-ray structure of **2**. Only the asymmetric unit is depicted. Ellipsoids are drawn at the 50% probability level.

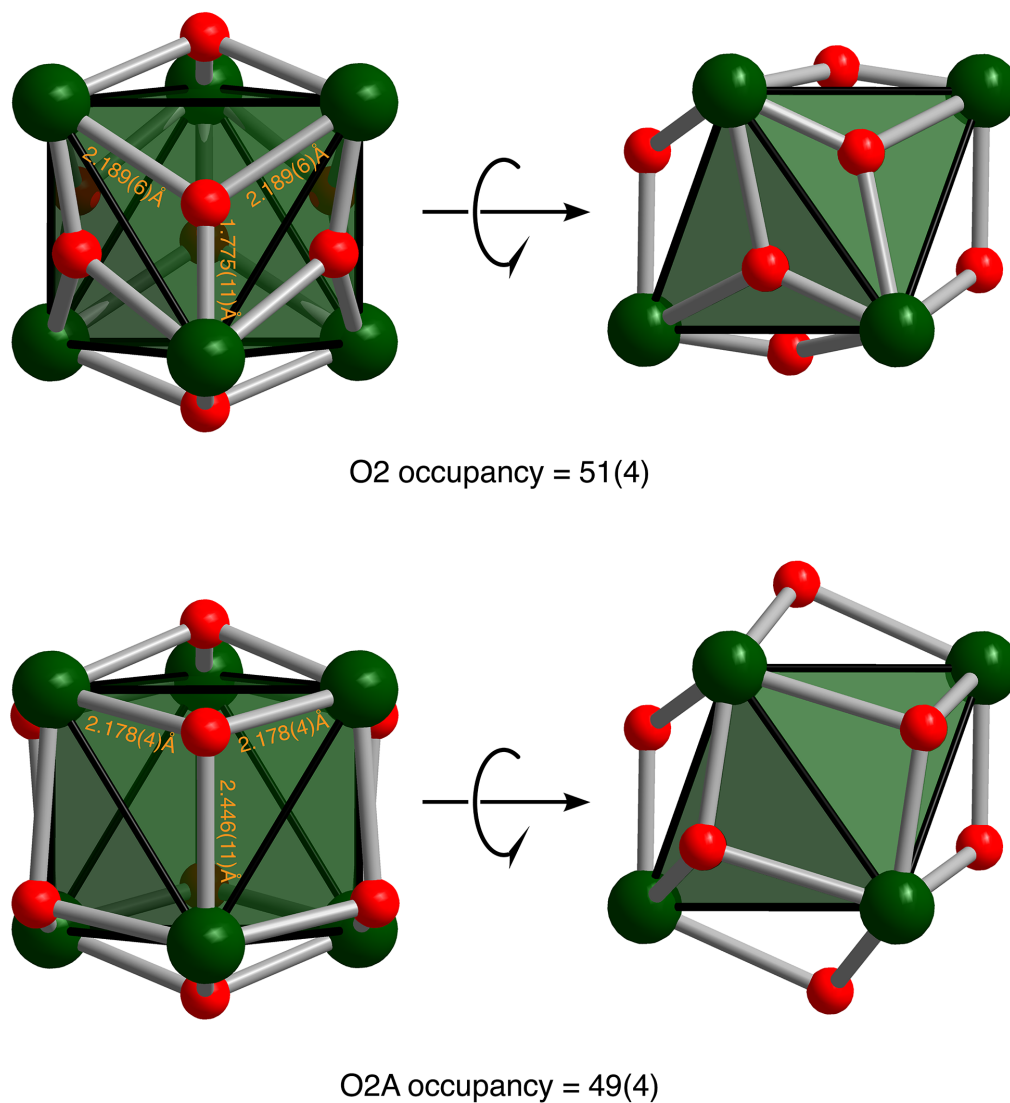
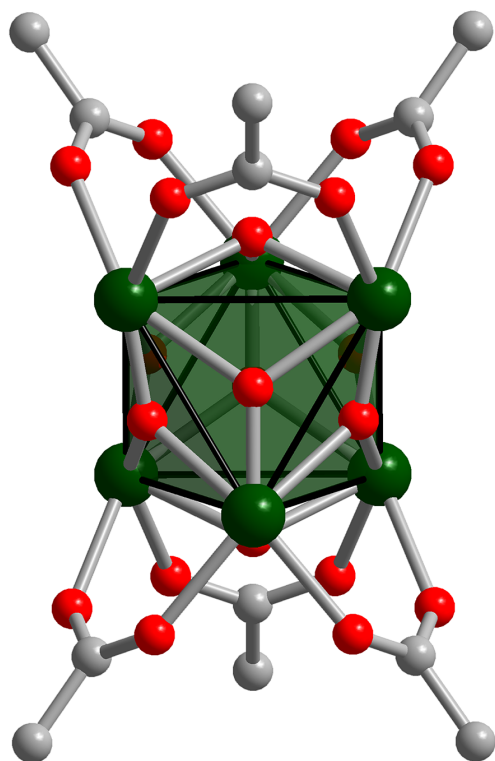
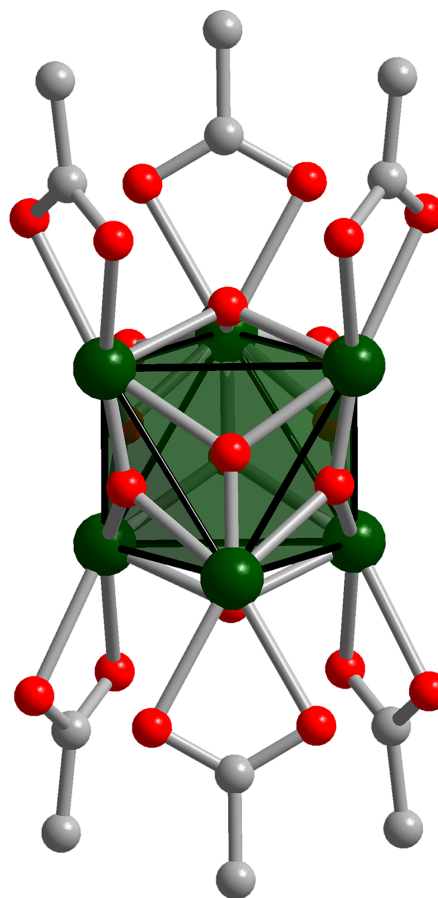


Figure S10. Disorder of the bridging oxygen atoms in the Zr_6 cluster in **1**. Green octahedra and red spheres represent the Zr_6 clusters and O atoms, respectively. Here, the bridging oxygen atom freely refines to two distinct positions, O2 and O2A. The near 50:50 occupancy reflects the stoichiometry of bridging oxo versus hydroxide ligands formulated in $[\text{Zr}_6\text{O}_4(\text{OH})_4]^{12+}$. The bridging oxygen atom in **1FeCl** similarly refines to these two positions with occupancies of 56(5):44(5).



$\mu\text{-CH}_3\text{CO}_2^-$
occupancy = 75(2)



$\kappa^2\text{-CH}_3\text{CO}_2^-$
occupancy = 25(2)

Figure S11. Single-crystal X-ray structure of the $[\text{Zr}_6\text{O}_4(\text{OH})_4(\text{CH}_3\text{CO}_2)_6]^{6+}$ cluster in **1**, depicting the μ -acetate (left) and κ^2 -acetate (right) binding modes. Green octahedra represent the Zr_6 clusters; gray and red spheres represent C and O atoms, respectively. The acetate ligands in **1FeCl** display occupancy the same respective binding modes at occupancies of 61(3):39(3).

Table S4. Terminal Zr–OH and Zr–OH₂ bond distances in crystallographically characterized 7-coordinate Zr⁴⁺ ions.^a

bond	<i>d</i> (Zr–O) (Å)	CSD refcode	ref
Zr–OH	1.952	TAQXEQ	20
	1.967		
	1.994		
	1.998		
	2.017		
	2.028		
	2.036		
	2.038		
average Zr–OH	2.00(4)		
Zr–OH ₂	2.161	NEDFAE	21
	2.181	NAYGIE	22
	2.196	TAQXEQ	20
	2.197	NEDDIK	21
	2.198	NEDDIK	21
	2.200	NEDDUW	21
	2.207	GOBPUJ	23
	2.210	GOBPUJ	23
	2.211	NEDDUW	21
	2.215	GOBQAQ	23
	2.218	NEDDUW	21
	2.221	HABLEB	24
	2.225	HABLEB	24
	2.231	NEDFAE	21
	2.251	GOBQAQ	23
	2.317	TAQXEQ	20
	2.317	AWUTIV	25
	2.329	PIBPOG	26
	2.335	AXELUK	27
average Zr–OH ₂	2.27(5)		

^aAs of CSD version 5.41, November 2019.

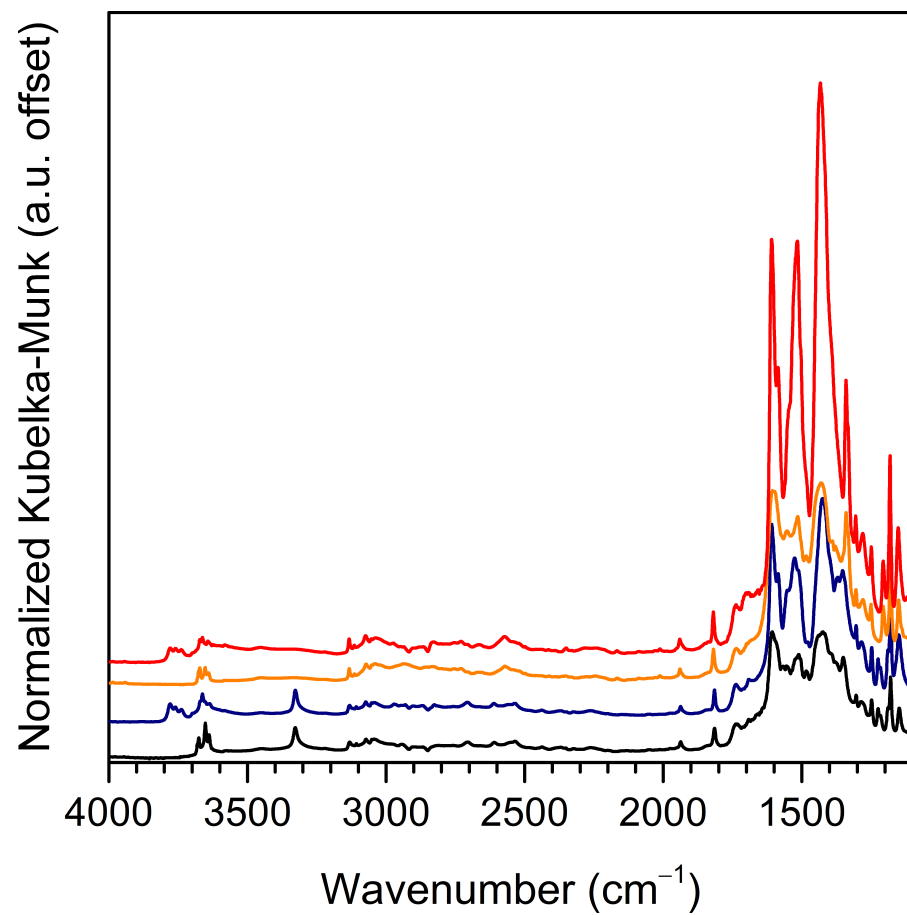


Figure S12. Full DRIFTS spectra of frameworks **1** (black), **2** (navy), **1FeCl** (orange), and **2FeCl** (red).

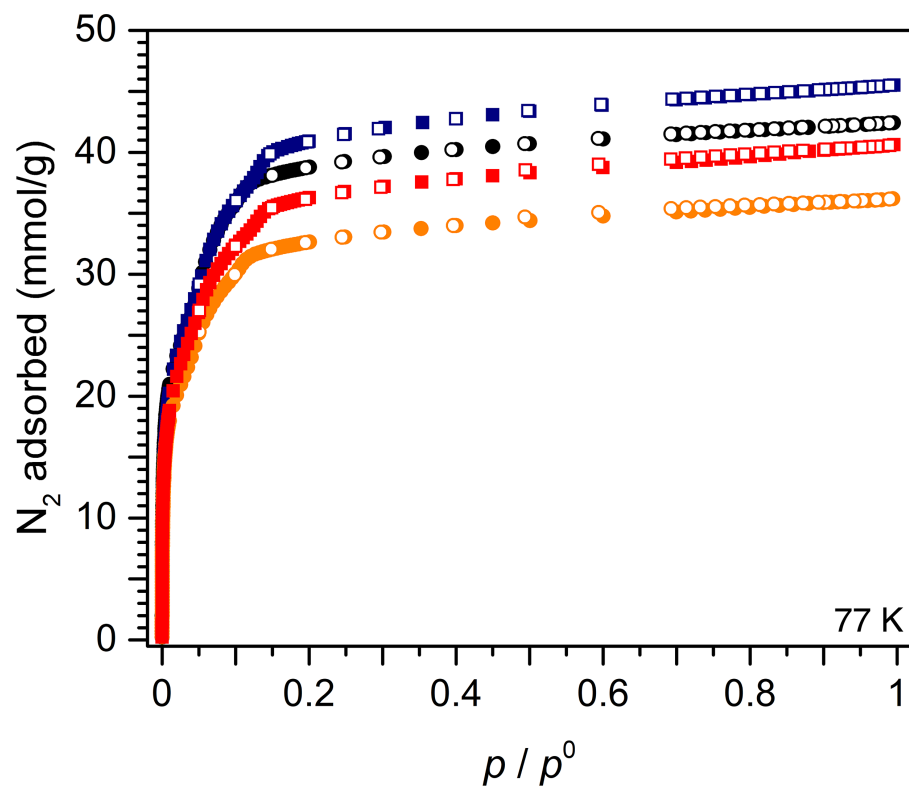


Figure S13. Nitrogen isotherms for frameworks **1** (black circles), **2** (blue squares), **1FeCl** (orange circles), and **2FeCl** (red squares) at 77 K. Solid and open symbols indicate adsorption and desorption data, respectively.

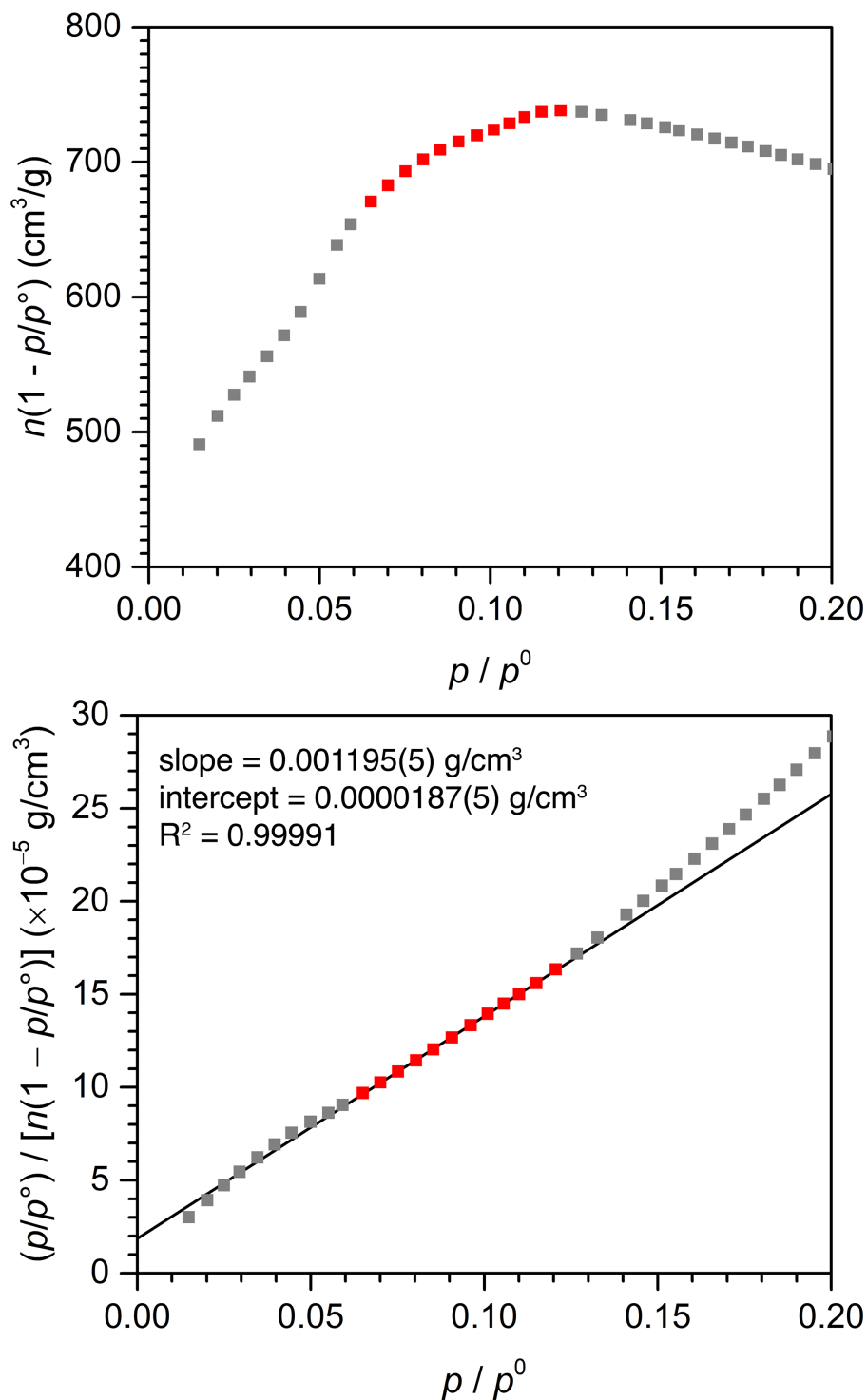


Figure S14. Determination of the BET surface area for **1**. Top: Plot of $n(1 - p/p^\circ)$ versus p/p° . The term $n(1 - p/p^\circ)$ monotonically increases over the range of $0.065 \leq p/p^\circ \leq 0.121$ (red squares), consistent with the second BET criterion. Bottom: Plot of $(p/p^\circ) / [n(1 - p/p^\circ)]$ versus p/p° . The best fit line affords a positive intercept and a positive C value, consistent with the first BET criterion. The gray squares indicate data that were not used to fit the BET equation.

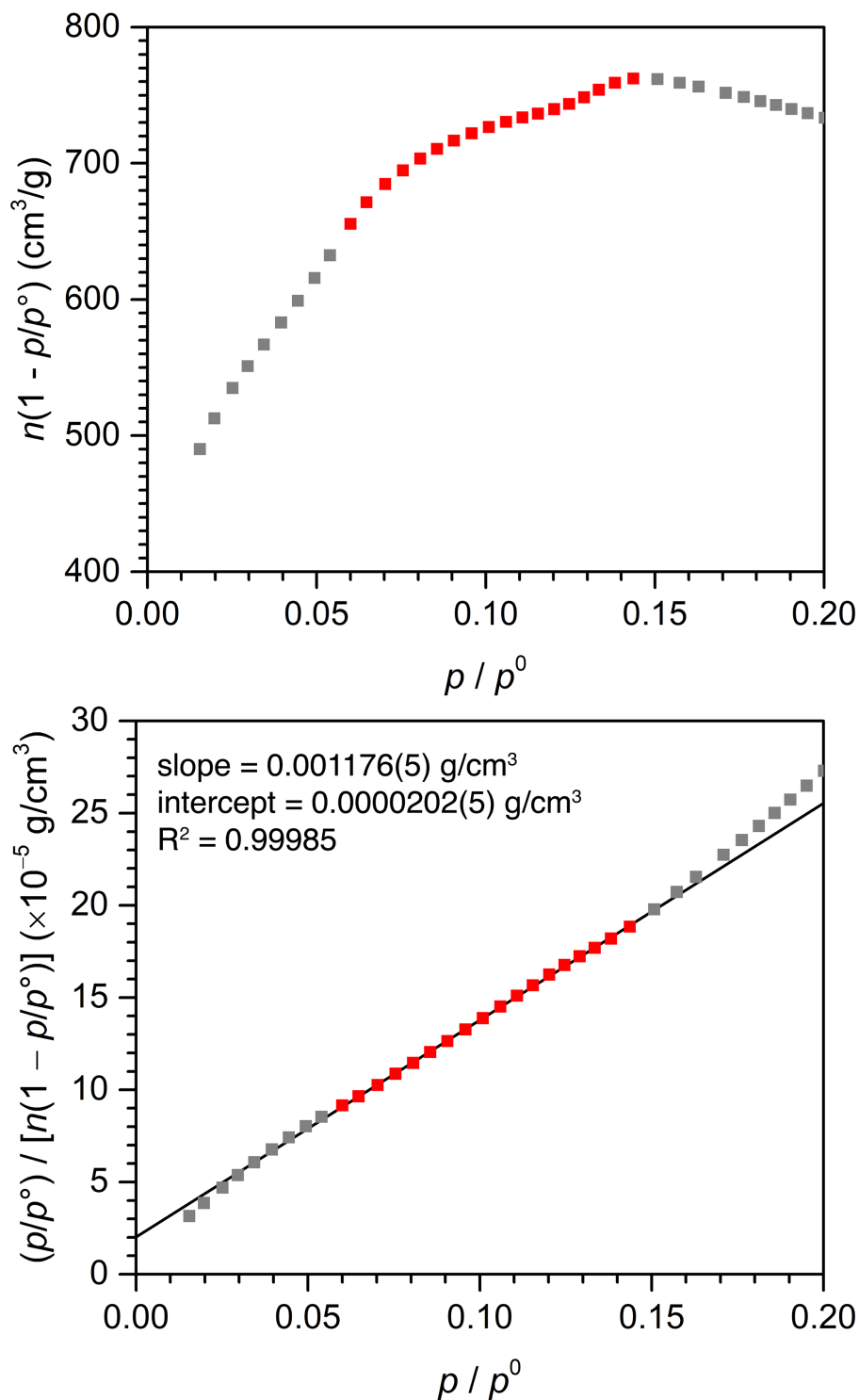


Figure S15. Determination of the BET surface area for **2**. Top: Plot of $n(1 - p/p^\circ)$ versus p/p° . The term $n(1 - p/p^\circ)$ monotonically increases over the range of $0.060 \leq p/p^\circ \leq 0.144$ (red squares), consistent with the second BET criterion. Bottom: Plot of $(p/p^\circ) / [n(1 - p/p^\circ)]$ versus p/p° . The best fit line affords a positive intercept and a positive C value, consistent with the first BET criterion. The gray squares indicate data that were not used to fit the BET equation.

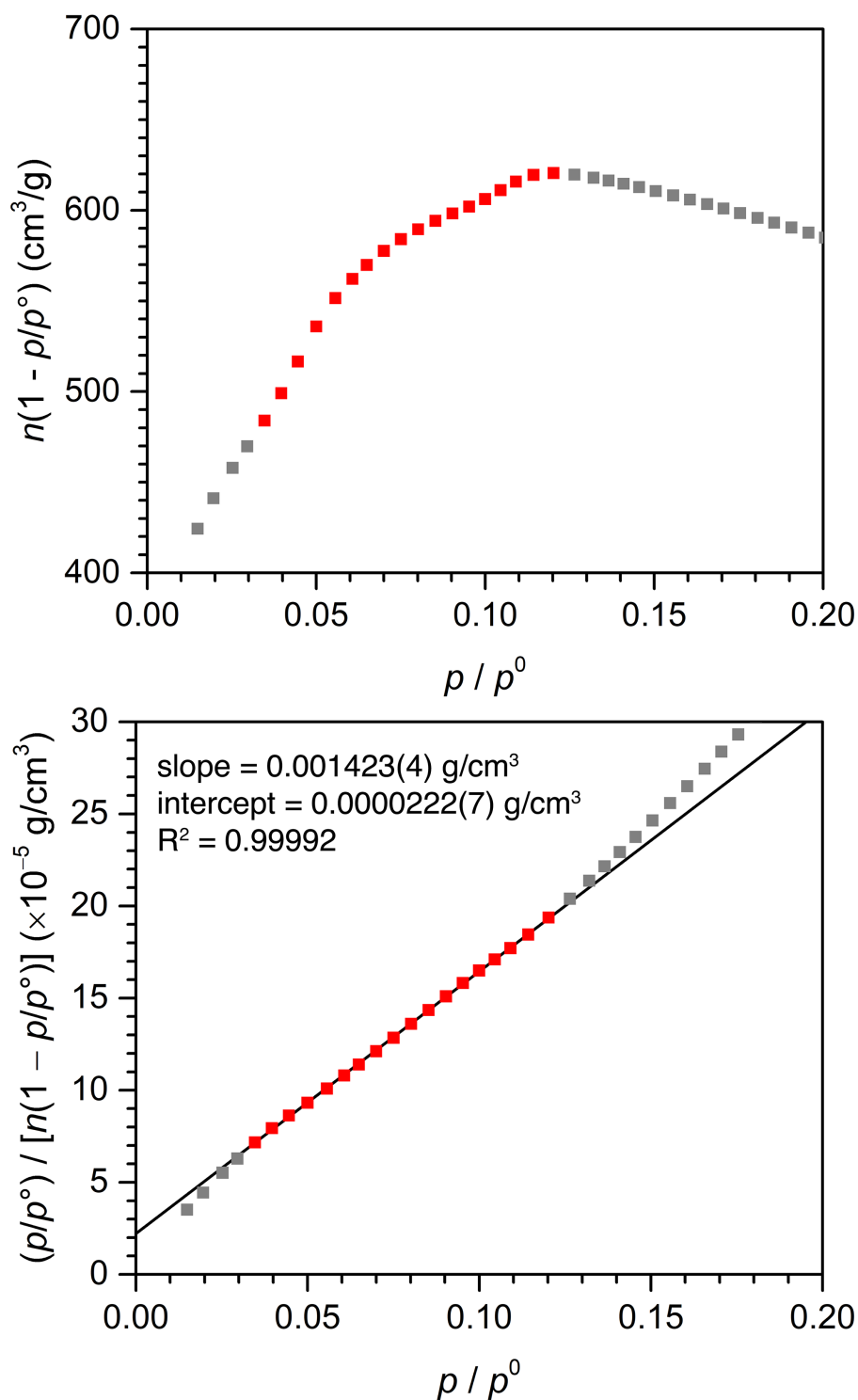


Figure S16. Determination of the BET surface area for **1FeCl**. Top: Plot of $n(1 - p/p^\circ)$ versus p/p° . The term $n(1 - p/p^\circ)$ monotonically increases over the range of $0.035 \leq p/p^\circ \leq 0.120$ (red squares), consistent with the second BET criterion. Bottom: Plot of $(p/p^\circ) / [n(1 - p/p^\circ)]$ versus p/p° . The best fit line affords a positive intercept and a positive C value, consistent with the first BET criterion. The gray squares indicate data that were not used to fit the BET equation.

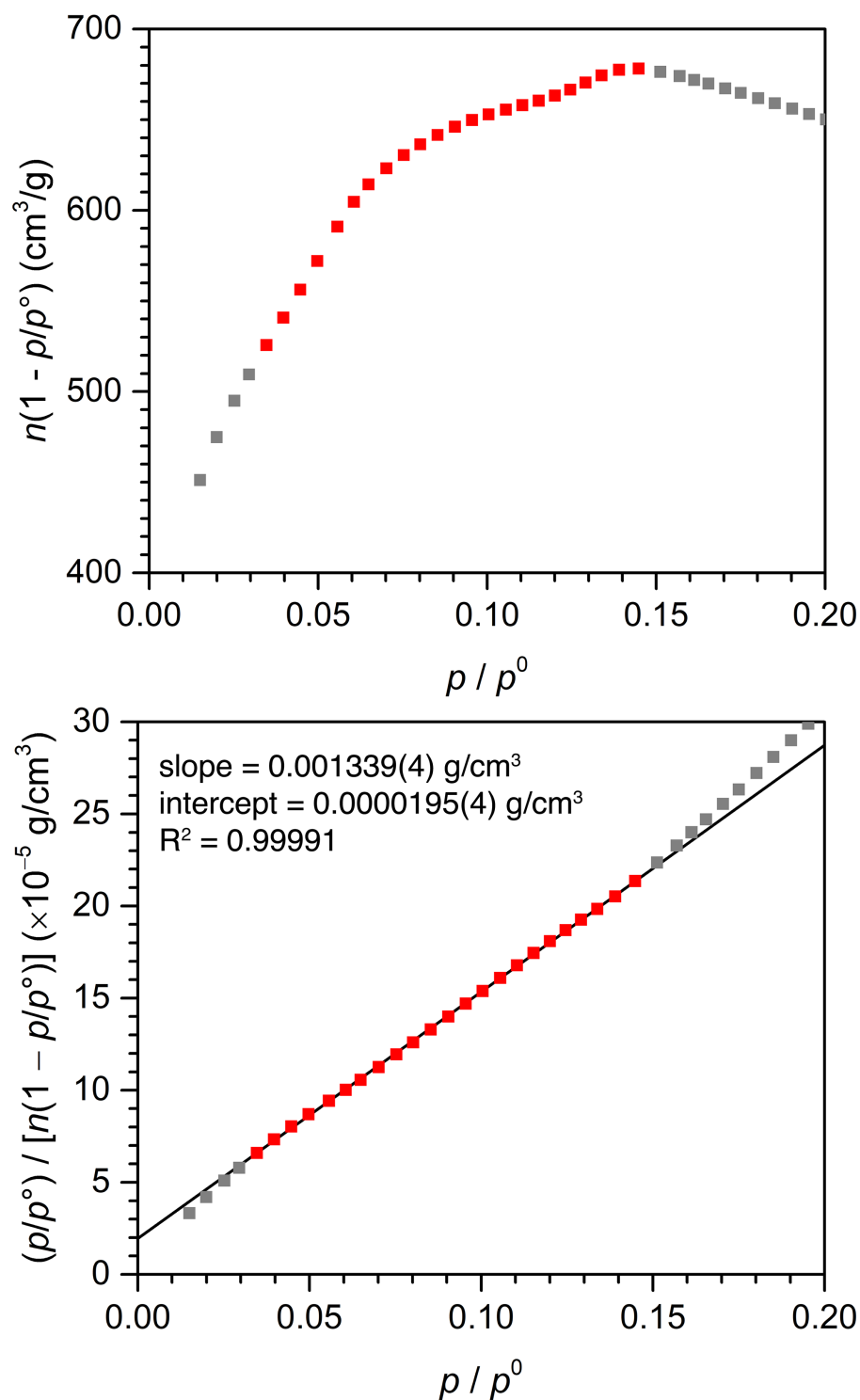


Figure S17. Determination of the BET surface area for **2FeCl**. Top: Plot of $n(1 - p/p^\circ)$ versus p/p° . The term $n(1 - p/p^\circ)$ monotonically increases over the range of $0.035 \leq p/p^\circ \leq 0.144$ (red squares), consistent with the second BET criterion. Bottom: Plot of $(p/p^\circ) / [n(1 - p/p^\circ)]$ versus p/p° . The best fit line affords a positive intercept and a positive C value, consistent with the first BET criterion. The gray squares indicate data that were not used to fit the BET equation.

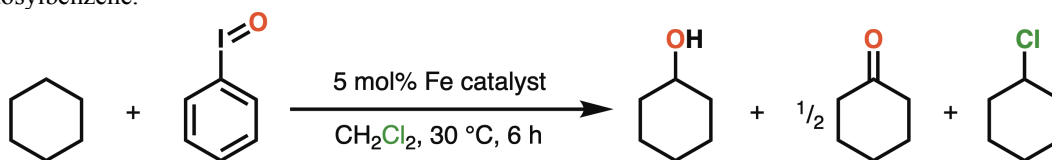
Table S5. Parameters and consistency criteria checks for BET surface area determinations in frameworks **1**, **2**, **1FeCl**, and **2FeCl**.

compound	n_m (cm ³ /g)	C	p/p° range fitted	$[p/p^\circ]n_m \pm 10\%$	$1/(\sqrt{C} + 1)$	BET surface area (m ² /g)
1	824	65	0.065–0.121	0.110 ± 0.11	0.110	3586(15)
2	836	59	0.060–0.144	0.117 ± 0.12	0.115	3638(16)
1FeCl	692	65	0.035–0.120	0.115 ± 0.12	0.110	3011(9)
2FeCl	736	70	0.035–0.144	0.108 ± 0.11	0.107	3204(9)

Table S6. Calculated N₂-accessible surface areas of frameworks **1**, **2**, and **1FeCl**.

compound	volumetric N ₂ -accessible surface area (m ² /cm ³)	density (g/cm ³)	gravimetric N ₂ -accessible surface area (m ² /g)
1	1828	0.508	3600
2	1595	0.444	3590
1FeCl	1783	0.546	3270

Table S7. Yields of cyclohexanol, cyclohexanone, and chlorocyclohexane in catalytic cyclohexane oxidation with iodosylbenzene.



catalyst	cyclohexanol yield ^a (%)	cyclohexanone yield ^b (%)	chlorocyclohexane yield ^c (%)	total yield ^d (%)	turnover number ^e
1FeCl	48(5)	17(5)	2.8(2)	68(8)	14(2)
2FeCl	24(5)	— ^f	1.7(2)	26(5)	5(1)
(TPP)FeCl	8(5)	— ^f	1.7(2)	9(5)	2(1)
1	— ^f	— ^f	— ^f	— ^f	0
1FeCl + CH ₃ OH ^g	8(3)	— ^f	— ^f	8(3)	1.7(5)
1FeCl + CH ₃ CO ₂ H ^g	0.6(3)	— ^f	0.8(7)	1(1)	0.3(2)
2FeCl + NBu ₄ OAc ^h	20(2)	— ^f	1.1(1)	22(2)	4.3(3)
FeCl ₃	— ^f	— ^f	9(2)	9(2)	1.8(3)

^aMoles of cyclohexanol / moles of iodosylbenzene. ^bMoles of cyclohexanone / moles of iodosylbenzene. ^cMoles of chlorocyclohexane / moles of iodosylbenzene. ^d(Moles of cyclohexanol + 2 × moles of cyclohexanone + moles of chlorocyclohexane) / moles iodosylbenzene. ^eTotal yield / moles of Fe. ^fBelow limit of detection. ^g2.00 mmol of methanol or acetic acid added. ^h0.200 mmol of NBu₄OAc added.

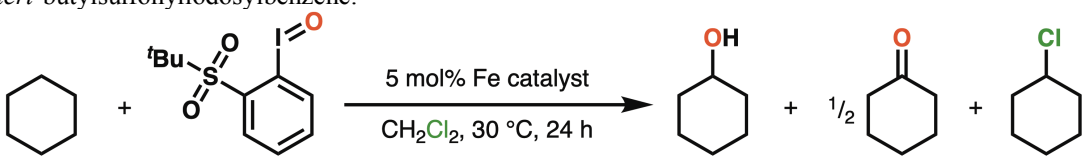
Table S8. Comparative activities of Fe and Mn porphyrin framework-based catalysts for cyclohexane oxidation.

framework	metal center (mol%) ^a	[C ₆ H ₁₂]	oxidant	reaction conditions	total yield ^b (%)	A/K ratio ^c	ref
1FeCl	Fe (5)	2 M	PhIO	CH ₂ Cl ₂ , 30 °C, 6 h	68(8)	5.6(3)	this work
PCN-221Fe	Fe (5)	neat	TBHP ^d	65 °C, 11 h	92.3	0.12	28
CZJ-1	Mn (2.5)	1 M	PhIO	CH ₃ CN, rt, ^e 20 h	94	0.11	29
MnRTMPyP	Mn (3.8)	neat	TBHP ^d	65 °C, 24 h	91.5	0.81	30
Fe-MMOF	Mn (10)	1 M	H ₂ O ₂	CH ₃ CN, rt, ^e 20 h	70	≤0.01	31
PIZA-3	Mn (10)	n.r. ^f	PhIO	CH ₃ CN, rt, ^e 2 h	47.8	8.9	32
ZnMnRPM	Mn (1)	1 M	^t BuSO ₂ PhIO	CH ₂ Cl ₂ , rt, ^e overnight	20	4.9	33
[(CH₃)₂NH₂] [Zn₂(HCOO)₂(Mn^{III}TCPP)] ·5DMF·2H₂O	Mn (6.7)	67 mM	PhIO	CH ₂ Cl ₂ , rt, ^e 6 h	20.6	0.73	34

^aMoles of catalytic metal sites / moles oxidant. ^b(Moles of cyclohexanol + 2 × moles of cyclohexanone + moles of chlorocyclohexane) / moles oxidant. ^cMoles of cyclohexanol / moles of cyclohexanone. ^dTert-butylhydroperoxide.

^eRoom temperature. ^fNot reported.

Table S9. Yields of cyclohexanol, cyclohexanone, and chlorocyclohexane in catalytic cyclohexane oxidation with 2-*tert*-butylsulfonyliodosylbenzene.

					
catalyst	cyclohexanol yield ^a (%)	cyclohexanone yield ^b (%)	chlorocyclohexane yield ^c (%)	total yield ^d (%)	turnover number ^e
1FeCl	10	— ^f	3.4	13.4	2.7
2FeCl	0.4	— ^f	— ^f	0.4	0.08
(TPP)FeCl	0.2	— ^f	— ^f	0.2	0.04
1	— ^f	— ^f	— ^f	— ^f	0

^aMoles of cyclohexanol / moles of iodosylarene. ^bMoles of cyclohexanone / moles of iodosylarene. ^cMoles of chlorocyclohexane / moles of iodosylarene. ^d(Moles of cyclohexanol + 2 × moles of cyclohexanone + moles of chlorocyclohexane) / moles oxidant. ^eTotal yield / moles of Fe. ^fBelow limit of detection.

References

1. Armarego, W. L. F.; Chai, C., Chapter 4 - Purification of Organic Chemicals. In *Purification of Laboratory Chemicals*, 7th ed.; Armarego, W. L. F.; Chai, C., Eds. Butterworth-Heinemann: Boston, 2013; pp 103–554.
2. Cardenal, A. D.; Park, H. J.; Chalker, C. J.; Ortiz, K. G.; Powers, D. C. cis-Decalin Oxidation as a Stereochemical Probe of in-MOF versus on-MOF Catalysis. *Chem. Commun.* **2017**, 53, 7377–7380.
3. Adler, A. D.; Longo, F. R.; Finarelli, J. D.; Goldmacher, J.; Assour, J.; Korsakoff, L. A Simplified Synthesis for meso-Tetraphenylporphine. *J. Org. Chem.* **1967**, 32, 476.
4. McKillop, A.; Kemp, D. Further Functional Group Oxidations Using Sodium Perborate. *Tetrahedron* **1989**, 45, 3299–3306.
5. Saltzman, H.; Sharefkin, J. G.; Newman, M. S.; Gill, N. Iodosobenzene. *Org. Synth.* **1963**, 43, 60.
6. (a) Krassowska-Řwiebocka, B.; Prokopienko, G.; Skulski, L. Biphasic Chlorination of Iodoarenes to (Dichloroiodo)arenes. *Synlett* **1999**, 1999, 1409–1410; (b) Song, F.; Wang, C.; Falkowski, J. M.; Ma, L.; Lin, W. Isorecticular Chiral Metal–Organic Frameworks for Asymmetric Alkene Epoxidation: Tuning Catalytic Activity by Controlling Framework Catenation and Varying Open Channel Sizes. *J. Am. Chem. Soc.* **2010**, 132, 15390–15398.
7. APEX3; Bruker, AXS Inc.: Madison, Wisconsin, USA, 2019.
8. SADABS; Bruker AXS Inc.: Madison, Wisconsin, USA, 2016.
9. Sheldrick, G. A Short History of SHELX. *Acta Crystallogr., Sect. A: Found. Crystallogr.* **2008**, 64, 112–122.
10. Sheldrick, G. Crystal Structure Refinement with SHELXL. *Acta Crystallogr., Sect. C: Struct. Chem.* **2015**, 71, 3–8.
11. Dolomanov, O. V.; Bourhis, L. J.; Gildea, R. J.; Howard, J. A. K.; Puschmann, H. OLEX2: A Complete Structure Solution, Refinement and Analysis Program. *J. Appl. Crystallogr.* **2009**, 42, 339–341.
12. WMOSS4: Mössbauer Spectral Analysis Software; Prisecaru, I.: www.wmoss.org, 2009.
13. Thommes, M.; Kaneko, K.; Neimark Alexander, V.; Olivier James, P.; Rodriguez-Reinoso, F.; Rouquerol, J.; Sing Kenneth, S. W. Physisorption of Gases, with Special Reference to the Evaluation of Surface Area and Pore Size Distribution (IUPAC Technical Report). *Pure Appl. Chem.* **2015**, 87, 1051–1069.
14. (a) Rouquerol, J.; Llewellyn, P.; Rouquerol, F., Is the BET Equation Applicable to Microporous Adsorbents? In *Studies in Surface Science and Catalysis*, Llewellyn, P. L.; Rodriguez-Reinoso, F.; Rouquerol, J.; Seaton, N., Eds. Elsevier: 2007; Vol. 160, pp 49–56; (b) Walton, K. S.; Snurr, R. Q. Applicability of the BET Method for Determining Surface Areas of Microporous Metal–Organic Frameworks. *J. Am. Chem. Soc.* **2007**, 129, 8552–8556; (c) Sing, K. S. W., Assessment of Surface Area by Gas Adsorption. In *Adsorption by Powders and Porous Solids*, 2nd ed.; Rouquerol, F.; Rouquerol, J.; Sing, K. S. W.; Llewellyn, P.; Maurin, G., Eds. Academic Press: Oxford, 2014; pp 237–268.
15. Willems, T. F.; Rycroft, C. H.; Kazi, M.; Meza, J. C.; Haranczyk, M. Algorithms and Tools for High-Throughput Geometry-Based Analysis of Crystalline Porous Materials. *Microporous Mesoporous Mater.* **2012**, 149, 134–141.
16. Ongari, D.; Boyd, P. G.; Barthel, S.; Witman, M.; Haranczyk, M.; Smit, B. Accurate Characterization of the Pore Volume in Microporous Crystalline Materials. *Langmuir* **2017**, 33, 14529–14538.

17. Bae, Y.-S.; Yazaydin, A. Ö.; Snurr, R. Q. Evaluation of the BET Method for Determining Surface Areas of MOFs and Zeolites that Contain Ultra-Micropores. *Langmuir* **2010**, *26*, 5475–5483.
18. Morris, W.; Voloskiy, B.; Demir, S.; Gándara, F.; McGrier, P. L.; Furukawa, H.; Cascio, D.; Stoddart, J. F.; Yaghi, O. M. Synthesis, Structure, and Metalation of Two New Highly Porous Zirconium Metal–Organic Frameworks. *Inorg. Chem.* **2012**, *51*, 6443–6445.
19. Babij, N. R.; McCusker, E. O.; Whiteker, G. T.; Canturk, B.; Choy, N.; Creemer, L. C.; Amicis, C. V. D.; Hewlett, N. M.; Johnson, P. L.; Knobelsdorf, J. A.; Li, F.; Lorscheid, B. A.; Nugent, B. M.; Ryan, S. J.; Smith, M. R.; Yang, Q. NMR Chemical Shifts of Trace Impurities: Industrially Preferred Solvents Used in Process and Green Chemistry. *Org. Process Res. Dev.* **2016**, *20*, 661–667.
20. Lin, H.; de Oliveira, P. W.; Huch, V.; Veith, M. Hydroxometalates from Anion Exchange Reactions of $[\text{BF}_4]^-$ based Ionic Liquids: Formation of $[\text{M}(\text{OH})_6]^{2-}$ (M = Ti, Zr) and $[\text{Zr}(\text{OH})_5]^-$. *Chem. Mater.* **2010**, *22*, 6518–6523.
21. Yi; Zhang, Q.-F.; Lam, T. C. H.; Chan, E. Y. Y.; Williams, I. D.; Leung, W.-H. Phosphato, Chromato, and Perrhenato Complexes of Titanium(IV) and Zirconium(IV) Containing Kläui's Tripodal Ligand. *Inorg. Chem.* **2006**, *45*, 328–335.
22. Il'in, E. G.; Kovalev, V. V.; Aleksandrov, G. G.; Grenthe, I. Dimeric Zirconium Tetrafluoride Complex $(\mu\text{-F}_2)\{\text{Zr}(\text{H}_2\text{O})[\text{OC}(\text{NMe}_2)_2\text{F}_3]\}_2 \cdot 2\text{H}_2\text{O}$: Strengthening of the Bond of the Axial Fluorine Atom. *Dokl. Chem.* **2005**, *401*, 42–46.
23. Fonari, M. S.; Kravtsov, V. C.; Simonov, Y. A.; Basok, S. S.; Ganin, E. V.; Gelmboldt, V. O.; Suwinska, K.; Lipkowski, J.; Alekseeva, O. A.; Furmanova, N. G. Crown-Templated Assembling of the Inorganic Binuclear Fluoro-Containing Anions in the System $\text{ZrO}_2/\text{HfO}_2$ ($\text{Nb}_2\text{O}_5/\text{Ta}_2\text{O}_5$)–HF– H_2O –Azacrown Ether. *Polyhedron* **2008**, *27*, 2049–2058.
24. Gao, Y.; Guery, J.; Jacoboni, C. Structures of $[\text{Zr}_2\text{F}_8(\text{dmsO})_4]$ and $[\text{ZrF}_4(\text{dmsO})(\text{H}_2\text{O})_2] \cdot 2\text{H}_2\text{O}$. *Acta Crystallogr., Sect. C: Struct. Chem.* **1993**, *49*, 963–965.
25. Wang, M.; Zhu, H.; Huang, D.; Jin, K.; Chen, C.; Sun, L. Salen-Type Zirconium Complexes with a Labile Coordination Site and a Robust Skeleton: Crystal Structure of $[(t\text{-Bu}_4\text{-Salen})\text{ZrCl}_2(\text{H}_2\text{O})]$. *J. Organomet. Chem.* **2004**, *689*, 1212–1217.
26. Liang, L.-C.; Chang, Y.-N.; Lee, H. M. Biphenolate Phosphine Complexes of Group 4 Metals. *Inorg. Chem.* **2007**, *46*, 2666–2673.
27. Watanabe, A.; Uchida, T.; Irie, R.; Katsuki, T. Zr[bis(salicylidene)ethylenediaminato]-Mediated Baeyer–Villiger Oxidation: Stereospecific Synthesis of Abnormal and Normal Lactones. *Proc. Natl. Acad. Sci. U. S. A.* **2004**, *101*, 5737–5742.
28. Feng, D.; Jiang, H.-L.; Chen, Y.-P.; Gu, Z.-Y.; Wei, Z.; Zhou, H.-C. Metal–Organic Frameworks Based on Previously Unknown Zr_8/Hf_8 Cubic Clusters. *Inorg. Chem.* **2013**, *52*, 12661–12667.
29. Xie, M.-H.; Yang, X.-L.; He, Y.; Zhang, J.; Chen, B.; Wu, C.-D. Highly Efficient C–H Oxidative Activation by a Porous Mn^{III} –Porphyrin Metal–Organic Framework under Mild Conditions. *Chem. Eur. J.* **2013**, *19*, 14316–14321.
30. Alkordi, M. H.; Liu, Y.; Larsen, R. W.; Eubank, J. F.; Eddaoudi, M. Zeolite-like Metal–Organic Frameworks as Platforms for Applications: On Metalloporphyrin-Based Catalysts. *J. Am. Chem. Soc.* **2008**, *130*, 12639–12641.

31. Zhang, W.; Jiang, P.; Wang, Y.; Zhang, J.; Zheng, J.; Zhang, P. Selective Oxidation Over a Metalloporphyrinic Metal–Organic Framework Catalyst and Insights Into the Mechanism of Bicarbonate Ion as Co-Catalyst. *Chem. Eng. J.* **2014**, *257*, 28–35.
32. Suslick, K. S.; Bhyrappa, P.; Chou, J. H.; Kosal, M. E.; Nakagaki, S.; Smithenry, D. W.; Wilson, S. R. Microporous Porphyrin Solids. *Acc. Chem. Res.* **2005**, *38*, 283–291.
33. Farha, O. K.; Shultz, A. M.; Sarjeant, A. A.; Nguyen, S. T.; Hupp, J. T. Active-Site-Accessible, Porphyrinic Metal–Organic Framework Materials. *J. Am. Chem. Soc.* **2011**, *133*, 5652–5655.
34. Zou, C.; Zhang, T.; Xie, M.-H.; Yan, L.; Kong, G.-Q.; Yang, X.-L.; Ma, A.; Wu, C.-D. Four Metalloporphyrinic Frameworks as Heterogeneous Catalysts for Selective Oxidation and Aldol Reaction. *Inorg. Chem.* **2013**, *52*, 3620–3626.